Received: 1 February 2022 | Revised: 17 May 2022 | Accepted: 2 July 2022

DOI: 10.1111/gbi.12523

ORIGINAL ARTICLE

gebiology WILEY

Exploring the secondary mineral products generated by microbial iron respiration in Archean ocean simulations

Christine Nims | **Jena E. Johnson**

Department of Earth and Environmental Sciences, University of Michigan, Ann Arbor, Michigan, USA

Correspondence
Jena E. Johnson, Department of Earth and Environmental Sciences, University of Michigan, 1100 North University Avenue, Ann Arbor, MI 48109, USA.
Email: jenaje@umich.edu

Funding information
National Aeronautics and Space Administration; U-Michigan Department of Earth and Environmental Sciences Scott Turner Award Funds

Abstract

Marine chemical sedimentary deposits known as Banded Iron Formations (BIFs) archive Archean ocean chemistry and, potentially, signs of ancient microbial life. BIFs contain a diversity of iron- and silica-rich minerals in disequilibrium, and thus many interpretations of these phases suggest they formed secondarily during early diagenetic processes. One such hypothesis posits that the early diagenetic microbial respiration of primary iron(III) oxides in BIFs resulted in the formation of other iron phases, including the iron-rich silicates, carbonates, and magnetite common in BIF assemblages. Here, we simulated this proposed pathway in laboratory incubations combining a model dissimilatory iron-reducing (DIR) bacterium, *Shewanella putrefaciens* CN32, and the ferric oxyhydroxide mineral ferrihydrite under conditions mimicking the predicted Archean seawater geochemistry. We assessed the impact of dissolved silica, calcium, and magnesium on the bioreduced precipitates. After harvesting the solid products from these experiments, we analyzed the reduced mineral phases using Raman spectroscopy, electron microscopy, powder x-ray diffraction, and spectrophotometric techniques to identify mineral precipitates and track the bulk distributions of Fe(II) and Fe(III). These techniques detected a diverse range of calcium carbonate morphologies and polymorphism in incubations with calcium, as well as secondary ferric oxide phases like goethite in silica-free experiments. We also identified aggregates of curling, iron- and silica-rich amorphous precipitates in all incubations amended with silica. Although ferric oxides persist even in our electron acceptor-limited incubations, our observations indicate that microbial iron reduction of ferrihydrite is a viable pathway for the formation of early iron silicate phases. This finding allows us to draw parallels between our experimental proto-silicates and the recently characterized iron silicate nanoinclusions in BIF chert deposits, suggesting that early iron silicates could possibly be signatures of iron-reducing metabolisms on early Earth.

KEYWORDS
banded iron formations, biomineralization, dissimilatory iron reduction, greenalite

1 | INTRODUCTION

Precambrian Banded Iron Formations (BIFs) are widespread iron- and silica-rich chemical sedimentary deposits that precipitated from anoxic, ferruginous seawater throughout the Archean Eon and Paleoproterozoic Era (Bekker et al., 2010; Farquhar et al., 2010; Johnson & Molnar, 2019; Cornelis Klein, 2005; Poulton & Canfeld, 2011). BIFs are often interpreted as illuminating records of Archean marine biogeochemical cycling, where chemical precipitates may have captured the intersection of ancient biological activity and seawater chemistry (Konhauser et al., 2017). The accurate identification of the primary BIF precipitates—and any evidence of early diagenetic reworking—is critical to reconstructing early seawater chemistry and deciphering the potential impact of microbial life on BIF formation, particularly in the absence of a robust fossil record (Knoll et al., 2016).

However, the complex and micron-scale BIF mineral assemblage often confuses the identification of primary versus secondary BIF mineral component(s). BIFs contain iron oxides (magnetite [Fe_3O_4] and hematite [Fe_2O_3]), iron silicates (greenalite [$(Fe)_3Si_2O_5(OH)_4$], riebeckite, and stilpnomelane), microcrystalline quartz ([SiO_2], also known as chert), and carbonates (siderite [$FeCO_3$], dolomite [$CaMg(CO_3)_2$], and ankerite [$Ca(Fe^{2+},Mg)(CO_3)_2$] (Bekker et al., 2014; Klein, 2005; Trendall, 2002). While ferric hydroxides [$Fe(III)(OH)_3$]) are widely hypothesized to be the initial BIF precipitate (e.g., Konhauser et al., 2017), much of the BIF assemblage likely derived from post-depositional processes including microbial respiration (Craddock & Dauphas, 2011; Heimann et al., 2010; Johnson et al., 2013; Konhauser et al., 2005; Walker, 1984), fluid-mediated reactions (Sun, Konhauser, et al., 2015), various grades of metamorphism (Bekker et al., 2014; Klein, 2005; Krapež et al., 2003; Trendall, 2002), and oxidizing fluids (Rasmussen et al., 2013, 2014). Despite efforts to distinguish the imprint of post-depositional processes on BIF mineral formation, the depositional environment, precursor phases, and the role of biology in BIF genesis remain disputed (Johnson et al., 2013; Johnson, 2019; Konhauser et al., 2017; Rasmussen et al., 2021; Tosca et al., 2019).

In an effort to resolve the initial BIF mineral, a series of studies recently utilized high-resolution petrography of BIF cherts to identify the original BIF phase(s) (Muhling & Rasmussen, 2020; Rasmussen et al., 2021; Sun, Konhauser, et al., 2015). Ubiquitous early-mineralizing chert in BIFs is often attributed to the estimated high dissolved silica concentrations in the Archean ocean (Siever, 1992), which lacked silica-secreting organisms (Maliva et al., 2005). The precompaction mineralization of low porosity chert (Fischer & Knoll, 2009; Krapež et al., 2003) makes it exemplary for the preservation of microfossils (Knoll et al., 2016; Maliva et al., 2005) and early minerals, either primary minerals (Rasmussen, Krapež, & Muhling, 2015) or early-forming diagenetic phases. Therefore, recent discoveries of widespread and abundant greenalite nanoinclusions in well-preserved 2.4 to 3.5 billion-year-old South African and Australian BIF cherts suggest that iron silicates were an important iron mineral in nascent BIF sediments (Muhling & Rasmussen, 2020; B. Rasmussen et al., 2021; Rasmussen, Krapež, & Muhling, 2015; Rasmussen, Krapež, Muhling, & Suvorova, 2015). Rasmussen et al. (2019) argue that the relatively uniform distribution and random orientations of these particles indicate that these iron silicate nanoinclusions were deposited as settling seawater precipitates and, therefore, were the primary BIF particles.

However, another proposed mechanism for the precipitation of early iron silicate minerals is through the microbial respiration of iron oxides in BIF sediments in the presence of high dissolved silica (Fischer & Knoll, 2009; Percak-Dennet et al., 2011; Robbins et al., 2019; Walker, 1984). Silicate minerals interpreted as early diagenetic precipitates forming in sedimentary porewaters also display random orientations in other Precambrian deposits (Lepot et al., 2017; Michalopoulos & Aller, 1995; Wacey et al., 2014), similar to the poorly defined orientation of iron aluminosilicate clays formed during simulated diagenesis of Amazon delta sediments (Michalopoulos & Aller, 1995). Furthermore, the preserved iron silicate inclusions in BIF cherts contain 10%–20% Fe^{3+} (Johnson et al., 2018), which could represent relict Fe(III) originating from initial iron oxide minerals reduced through post-depositional iron respiration (Johnson, 2019; Johnson et al., 2018). Dissimilatory iron reduction (DIR) is an anaerobic respiratory metabolism, performed by a variety of microbes, that couples the oxidation of organic carbon with the reduction of Fe(III) substrates (Lovley and Phillips, 1988; Kato et al., 2019; Myers & Nealson, 1990; Miot & Etique, 2016) as in Reaction (1), using CH_2O as a simplified formula for organic carbon:

$$4Fe(OH)_3 + 7H^+ + CH_2O \rightarrow 4Fe^{2+} + HCO_3^- + 10\,H_2O. \quad \text{(Reaction 1)}$$

This paired iron- and carbon-cycling metabolism has been suggested as both the progenitor of iron formation carbonates, where $Fe(II)CO_3$ precipitated from porewaters saturated in Fe(II) and inorganic carbon, and as an explanation for the lack of organic carbon in Precambrian BIFs (Baur et al., 1985; Craddock & Dauphas, 2011; Heimann et al., 2010; Johnson et al., 2008; Konhauser et al., 2005; Walker, 1984). Likewise, microbial iron respiration in the high-silica pore waters of Archean sediments could have produced secondary iron silicate biominerals, as proposed by Fischer and Knoll (2009), through the saturation of Fe(II) and dissolved silica.

Extensive DIR research describes the diverse secondary minerals associated with microbial iron respiration (further details in Supporting Information). While this prior microbial iron reduction work displays a spectrum of DIR-mediated mineral products, ranging from secondary Fe(III) oxides to Fe(II,III) phases such as magnetite or an Fe(II,III) green rust salt (e.g., Bae & Lee, 2013; Etique et al., 2016; Han et al., 2020; O'Loughlin et al., 2019; Salas et al., 2009; Zegeye et al., 2010), the absence of dissolved silica in these studies decouples their mineral observations from predictions of ancient DIR products in the siliceous geochemistry of Archean seawater.

A limited set of experimental and environmental DIR investigations have included dissolved silica or used silicate minerals as Fe(III) substrates (e.g., Dong et al., 2009; Kostka et al., 1999; O'Reilly, 2005; Phoenix et al., 2003; Sergent et al., 2011); see Supporting Information

for more details. Notably, Komlos et al. (2007) detected putative secondary Fe(II) silicates by Mössbauer spectroscopy but used aluminosilicate clay minerals as a starting iron substrate. While this earlier DIR work explored clay-microbe interactions and the impact of silicic acid on iron reduction, the results of many silica-amended DIR experiments are ill-suited for comparison to the Archean environment due to their incongruent sources of silica, such as sand or clay minerals, and/or the addition of other improbable Archean chemical species, like organic or phosphate buffers.

Additionally, ancient seawater composition likely varied from the experimental conditions employed in the vast majority of DIR studies. Recent models suggest the Archean ocean had [Si_{aq}] = 0.67 to 2 mM (Jones et al., 2015; Konhauser et al., 2007; Maliva et al., 2005; Siever et al., 1992), a circumneutral pH of 6.5–7.5 (Halevy & Bachan, 2017; Jones et al., 2015; Krissansen-Totton et al., 2018) and approximately 10 mM dissolved inorganic carbon (DIC) ca. 2.5 Ga (Halevy & Bachan, 2017). Generally, calcium [Ca^{2+}] estimates in Archean seawater are analogous to the modern ocean concentration of 10 mM (Higgins et al., 2009; Holland, 1984), though other recent estimates suggest higher [Ca^{2+}] concentrations of 35–40 mM (Jones et al., 2015) or 50–100 mM (Halevy & Bachan, 2017).

Research investigating DIR in simulated ancient marine conditions remains limited. Studies replicating Archean environmental conditions mainly focused on distinguishing the BIF Fe isotopic signals during Fe(III) oxide respiration in the presence of dissolved silica (Wu et al., 2009) and during respiration of Si–Fe(III) gels (Percak-Dennet et al., 2011), as well as the implications of DIR of Si–Fe(III) gels on Si isotope fractionation (Reddy et al., 2016). However, these isotope-centered studies did not characterize the secondary mineral products from DIR of Fe(III)-Si gels in artificial Archean seawater, with the exception of reporting a singular, putative smectite mineral (Percak-Dennet et al., 2011). Moreover, this tentatively identified three-layered silicate phase is distinct from the two-layer early greenalite minerals hosted in BIF cherts. Additionally, these prior Archean-like DIR studies were completed at an elevated pH of 8.7 (Wu et al., 2009) or high DIC concentrations (≥30 mM) (Percak-Dennet et al., 2011; Reddy et al., 2016). In another set of Archean-relevant experiments that characterized DIR-promoted Ca/Fe-carbonate mineral precipitation (Zeng & Tice, 2014), the experimental matrix lacked dissolved silica. Thus, a more extensive biomineral evaluation of DIR products in simulated Archean seawater, with high levels of silica, is essential to understanding whether DIR could be responsible for the genesis of early iron silicate minerals in BIFs. Despite the range of previously explored experimental conditions, no study has heretofore demonstrated the formation of authigenic Fe(II)-iron silicates as a secondary mineral product of Fe(III) oxide respiration.

In this study, we used batch experiments to examine and characterize the secondary phases that form after microbial iron reduction, as performed by a model iron-reducing bacterium, with synthesized ferrihydrite as the electron acceptor and lactate as the electron donor across a range of Archean-relevant chemistries. Specifically, we tested the impact of dissolved silica and divalent cations (calcium and magnesium) on the products from microbial reduction of ferrihydrite in conditions representative of Archean marine environments. Our exploration of DIR secondary mineral precipitates reveals how the interplay of iron, dissolved silica, and divalent cations can alter the products of microbial iron respiration, including the formation of potential precursor iron silicates.

2 | METHODS

We designed a matrix of experiments to test the effects of dissolved Si, Ca^{2+}, and Mg^{2+} on the products of DIR of ferrihydrite, alongside abiotic control incubations, in a solution chemistry mimicking the Archean ocean. Though constrained by Archean-like marine geochemistry, our set-up aimed to maximize the extent of iron reduction to explore the possible formation of Fe(II)-rich silicate phases. Therefore, we performed laboratory-based experiments with low concentrations of ferrihydrite (1.5 mM), more analogous to marine water column environments, and high concentrations of lactate (30 mM), both an organic substrate and a concentration that would not be expected in water column or sedimentary environments in Archean ocean basins but likely to fuel more extensive DIR in these experiments. These experiments incubated for >4.5 months (19 weeks) to allow ample time for microbial iron reduction, subsequent precipitation, and low-temperature recrystallization reactions, optimizing suitable conditions for the formation of iron silicates.

2.1 | Preparation of the artificial Archean seawater (AAS) medium

We prepared artificial seawater medium (AAS), adapted from Hinz et al. (2021), Percak-Dennet et al. (2011), and Reddy et al. (2016), in an anaerobic chamber/glovebox using autoclaved anoxic ultrapure Milli-Q water in borosilicate bottles (see additional details in the Supporting Information). The artificial seawater medium (AAS) was modified with lower concentrations of bicarbonate, magnesium (when added), and ammonium to mimic the conditions constrained by models of Neoarchean ocean geochemistry (Halevy & Bachan, 2017; Jones et al., 2015; Krissansen-Totton et al., 2018). Phosphate was excluded from the medium to preclude the spontaneous precipitation of highly insoluble iron phosphates (Fredrickson et al., 1998; Jorand et al., 2000) not observed in the rock record. The final basal medium contained the following: 400 mM sodium chloride (NaCl), 9 mM potassium chloride (KCl), 1 mM ammonium chloride (NH_4Cl). The medium was further amended with and buffered by 10 mM sodium bicarbonate ($NaHCO_3$) and supplemented with amino acids (glutamine, serine, and arginine, 20 μg mL^{-1}, [Myers & Nealson, 1990]), 1 mL L^{-1} SL-10 trace minerals (Widdel et al., 1983) and 1 mL L^{-1} vitamin solution (Balch & Wolfe, 1976). The medium was additionally augmented with 30 mM sodium lactate ($NaC_3H_5O_3$) as the electron donor, in substantial excess of the concentration required to reduce 1.5 mM Fe(III) (similar to Kukkadapu et al., 2004; Percak-Dennet

et al., 2011). We used this organic carbon concentration to prevent any electron donor limitation in the microbial reduction experiments and promote more extensive reduction despite possible phosphate limitation.

This basal AAS medium was subdivided into two solutions with and without the addition of 1 mM dissolved silica dispensed from anoxic and filtered sodium metasilicate stock (Na_2SiO_3, Sigma Aldrich). The medium was then partitioned into eight separate autoclaved 250 ml Kimax bottles to test the effects of each cation in the presence and absence of silica: 10 mM $CaCl_2$, 10 mM $MgCl_2$, 10 mM $MgCl_2$ and 10 mM $CaCl_2$ combined, and a condition without added cations. The pH was measured and reset to pH ~7 if needed using 3 M HCl.

2.2 | Preparation of DIR model microbe and ferrihydrite

Frozen stocks of *Shewanella putrefaciens* CN32 (ATCC strain BAA-453) stored at −80°C in 25% glycerol were revived in tryptic soy broth (TSB) (Bacto Tryptic Soy Broth, BD) at pH 7 (±0.5) at 25°C in a shaking incubator at 150 rpm. We washed cell slurries three times in a 0.22 µm filter-sterilized salt solution composed of 400 mM NaCl, 10 mM KCl, 1 mM NH_4Cl to remove organic residues from the TSB broth.

We synthesized a ferrihydrite substrate using a method adapted from Sklute et al. (2018) (details in Supporting Information). Small subsamples of the ferrihydrite were characterized by Raman spectroscopy and measured by the Ferrozine assay to calculate the total iron concentration of the initial ferrihydrite stock dispensed into experimental vessels (see Section 2.4 for details).

2.3 | Experimental procedure

Synthesized ferrihydrite was dispensed into 80 ml autoclaved serum bottles on the benchtop to a final concentration of approximately 1.5 mM. All serum bottles containing ferrihydrite were loosely capped with sterile foil and were transferred into the anoxic glovebox and then allowed to equilibrate with the N_2 environment. Previously prepared anoxic AAS solutions were brought into the glovebox and 35 ml of specific batch medium was pipetted into each respective serum bottle containing ferrihydrite. All bottles were sealed with a butyl stopper and aluminum crimp.

After removing the serum bottles from the glovebox, we added 5 ml of the *S. putrefaciens* cell suspension (12.5% inoculum) to bring each bottle to a final volume of 40 ml. The optical density (OD) of the inoculum cell suspension was 0.337 at 600 nm (Genesys 50 UV–Vis spectrophotometer, Thermo Fisher), roughly translating to 10^7–10^8 cells/ml per bottle (Biffinger et al., 2008). Incubations were run in triplicate along with an abiotic control at each condition. The serum bottles were placed in a dark incubator at 31°C, the optimal growth temperature for *S. putrefaciens* CN32 (Pakchung et al., 2008) to maximize microbial iron reduction. The bottles were lightly agitated manually twice a month to homogenize solution conditions but were otherwise undisturbed for a total duration of 19 weeks.

At the end of the bioreduction experiment, samples of the solid precipitates and aliquots of solutions from each condition were harvested in the glovebox (details in Supporting Information). Final pH was measured upon the disassembly of each experiment (see Table S1). Subsamples of final solutions and solids were acquired from two separate replicate bioreduction experiments to measure iron concentrations and redox speciation in DIR solutions and solids. We additionally collected two technical replicates from the final solution and solids from each control condition for iron concentration and redox analyses. Solution subsamples from each (triplicate) biotic experiment and control experiment were collected to determine final Si concentrations. Additional subsamples of solids were extracted from all experiments, centrifuged in sterile epitubes, and rinsed three times with anoxic, ultrapure water to enable mineralogical characterization. All solid and solution samples were stored in epitubes, individually sealed in Mylar bags in an N_2 atmosphere, and then transferred into a −80°C freezer for preservation until analysis.

2.4 | Solution and precipitate characterization

We employed two colorimetric assays to determine both the Fe concentrations and the Si concentrations of our final experimental solutions. We additionally determined the iron redox distribution of the experimental precipitates from each condition. To confirm the initial mineralogy, redox state, and estimate the starting Fe(III) concentration, we examined the synthesized ferrihydrite using Raman spectroscopy and the Ferrozine assay (Stookey, 1970; Viollier et al., 2000). This characterization confirmed the synthesized precipitate was indeed ferrihydrite with >97% Fe(III) (Figure S1A, ferrozine data are not shown; details in Supporting Information). Fe(II)/Fe(III) speciation and the Fe concentration of post-incubation solutions, control solutions, and solids from all experimental conditions were additionally determined using the Ferrozine assay. To describe the partitioning of Fe/Fe redox in the solution and solid experimental subsamples, we describe the pool of soluble, aqueous Fe(II) measured in final experimental solutions as $Fe(II)_{aq}$ and $Fe(II)/FeT_{solid}$ (where FeT signifies the total iron measured) as the redox state of iron extracted from solid experimental precipitates. The Si concentration of experimental solutions at the conclusion of the incubations (Si_{aq}) were determined using the silicomolybdate colorimetric assay (details in Supporting Information).

The solid products were further characterized using scanning electron microscopy (SEM) analyses. Pre-rinsed precipitates were thawed and dispensed (15 µl) onto carbon tape atop aluminum stubs and allowed to dry in the glovebox. Dried samples were immediately transported to a Denton Desk II vacuum coater and sputtered with Au for 100 s for a coating of approximately 10–20 nm. We collected secondary electron images of mineral precipitates using a JEOL JSM-7800FLV SEM system operating at an accelerating voltage of 10–15 kV and a working distance of 10 mm. Qualitative elemental

maps and spectra using energy-dispersive spectroscopy (EDS) were obtained using an Oxford XMaxN 80 mm^2 silicon-drift energy-dispersive X-ray spectrometer. Spectra were processed using OXFORD AZTEC v3.3 software.

Transmission electron microscopy (TEM) analyses were conducted on representative subsamples of each experimental condition. For TEM preparation, mineral residues were thawed in the glovebox and resuspended in anoxic Milli-Q water prior to being pipetted onto a Cu grid with a Formvar lacey support film. Scanning TEM (STEM) imaging and analysis used an FEI Talos F200X G2 STEM system equipped with a Gatan OneView 4K camera, operating at an accelerating voltage of 200 kV. We characterized the morphology and elemental chemistry of nano- and microscale mineral precipitates by bright-field TEM and high-angle annular dark-field (HAADF) STEM imaging, respectively. Qualitative EDS spectra were collected with a Super-X window-less detector and processed with the Velox platform. Selected area electron diffraction (SAED) patterns and high-resolution TEM (HRTEM) imaging enabled the mineral identification of imaged particles. Fast Fourier-transforms (FFTs) of lattice fringes captured in HRTEM images facilitated the determination of mineral d-spacing. All bright-field, HRTEM images, and SAED patterns were analyzed using GATAN DIGITAL MICROGRAPH software.

We additionally applied Raman spectroscopy to our experimental precipitates to confirm the identification of mineral products. Raman microspectroscopy measurements were taken on a Horiba XploRA PLUS Raman system, with spectra were collected at ambient conditions using a laser excitation of 532 or 785 nm (see Supporting Information for details on Raman measurements). The 785 nm laser was selected for the bioreduced samples due to the resonant Raman effect of the 532 nm laser with c-type cytochromes (Virdis et al., 2014; Wolf et al., 2018), common membrane proteins in *S. putrefaciens*. We compared our Raman spectra against iron oxide phases from Sklute et al. (2018), iron and calcium carbonate reference standards, and internal lab standards for iron silicate minerals (greenalite, cronstedtite, and minnesotaite). The standards for calcite (#R040070) and aragonite (#R040078) were sourced from the RRUFF database (Lafuente et al., 2016).

Powder X-ray Diffraction (XRD) analysis permitted the interrogation of the crystalline phases in a subsample of each experimental product under anoxic conditions. 2D XRD data was collected using a Bruker D8 DISCOVER with Vantec500 area detector equipped with a Cu Kα source at the McMaster Analytical X-Ray Diffraction Facility (MAX) in Ontario, Canada. Diffraction patterns were plotted in OriginPro and compared with mineral standards obtained from the RRUFF database.

2.5 | Saturation calculations

We used Visual MINTEQ 3.1 to calculate the activities of solutes in our experimental solutions and determine the mineral saturation indices at the initiation and termination of our incubations. Saturation indices, SI, of mineral phases were calculated by comparing the product of the chemical activities of the dissolved ions that comprise each possible mineral with the thermodynamic solubility product of the relevant mineral. We used the measured pH values and an approximate final $Fe(II)_{aq}$ for post-DIR taken from the highest measured final $Fe(II)_{aq}$ by Ferrozine, but all other ions were set to the initial concentrations. For example, the SI of carbonate phases was determined following Equation (1) below:

$$SI = \log\left(\frac{\left(a_{M^{2+}}\right)\left(a_{CO_3^{2-}}\right)}{K_{sp}}\right) \quad (1)$$

Where a is calculated activity in the media, M^{2+} signifies Fe^{2+} or Ca^{2+} for siderite or calcium carbonate (calcite or aragonite), respectively, and K_{sp} is the solubility product of the chosen mineral.

3 | RESULTS

3.1 | Solution and precipitate chemistry

All experiments initiated at a pH of 7 ± 0.1. After the 19-week incubation, we found that the pH of bioreduced experiments increased an average of 0.7 and control experiments increased 0.9 compared to pre-incubation pH measurements (Table S1). Both inoculated and control experiments with silica showed substantial pH increases, but this effect was diminished in experiments containing calcium.

The final dissolved silica concentrations determined by the silicomolybdate assay varied by experimental condition and emphasized the complexities of the combined influence of silica and divalent cations on DIR in Archean-like solutions (Figure 1c, Table S2). Incubations of *S. putrefaciens* amended with 1 mM silica and the combined cations contained the highest mean concentration of dissolved Si remaining at the conclusion of the experiments ($[Si_{aq}]$ = 848 μM). Dissolved Si in inoculated, silica-amended experiments containing either calcium or magnesium depleted silica to a similar amount, at 571 and 603 μM, respectively. The solution in the inoculated AAS-only experiments amended with silica indicated the greatest depletion of silica from solution ($[Si_{aq}]$ = 507 μM) (Table S2). Control experiments with amended Si showed a depletion of ~30%–40% silica, apart from an anomalously low value in the magnesium-bearing control experiment (Figure 1c). Overall, the experimental conditions with amended Si indicated a shift from initial dissolved Si to silica incorporation into precipitates. Experiments without amended silica showed a low accumulation of Si_{aq} of approximately 105 μM in control experiments and 173 μM in experiments with *S. putrefaciens*, which could be attributed to the leaching of borosilicate glass (Frankel et al., 2018) during autoclaving, sparging while boiling, or the 19 week incubation at 31°C (Figure 1c).

Overall, our Ferrozine measurements demonstrated a strong effect of silica on the final concentration of dissolved $Fe(II)_{aq}$. We observed a higher total measured $Fe(II)_{aq}$ in the final solutions of inoculated experiments without added dissolved silica,

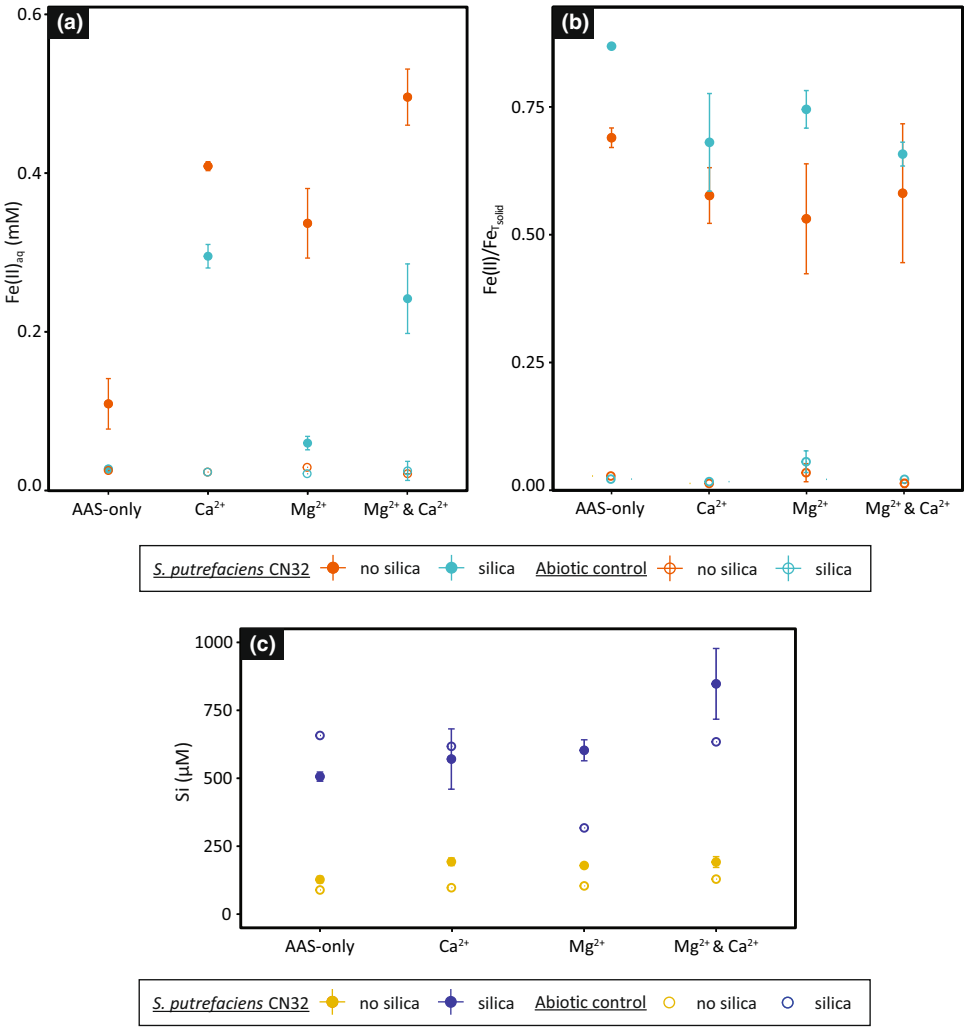

FIGURE 1 Ferrozine measurements of (a) $Fe(II)_{aq}$ and (b) $Fe(II)/FeT_{solid}$ (where FeT signifies the total iron measured) of solid precipitates in both inoculated experiments and controls at culmination of the bioreduction experiment. Data points represent means and error bars indicate one standard deviation of two replicates. Silicomolybdate assay results of (c) final aqueous silica concentrations in each experiment (Si_{aq}). Data points represent means and error bars indicate one standard deviation of three replicates.

averaging ~0.2 mM higher relative to their silica-amended counterparts (Figure 1a; Table S3). In these conditions without added silica, experiments with calcium or magnesium cations demonstrated even higher $Fe(II)_{aq}$ compared to the samples without these divalent cations (Figure 1a). The combined cation experiment without amended silica had roughly 5× higher $Fe(II)_{aq}$ (mean = 0.50 mM) than the $Fe(II)_{aq}$ present in the AAS-only samples (mean = 0.11 mM).

While all silica-augmented experiments had lower $Fe(II)_{aq}$, the magnesium- and magnesium–calcium-supplemented conditions concluded with considerably lower $Fe(II)_{aq}$ than the same conditions without added silica (Figure 1a). Magnesium-bearing inoculated experiments without amended silica had $Fe(II)_{aq}$ ([Fe(II)] = 0.34 mM) that decreased dramatically in the presence of added silica ($[Fe(II)_{aq}]$ = 0.06). The combined cation experiment with amended silica had nearly 50% less $Fe(II)_{aq}$, with a [Fe(II)] of 0.24 mM compared to 0.50 mM Fe(II) without added Si. In contrast, the calcium-supplemented solutions had the highest $Fe(II)_{aq}$ concentration of all of the siliceous experiments ([Fe(II)] = 0.30 mM), a value proximal to the $Fe(II)_{aq}$ in the calcium solution lacking added silica ([Fe(II)] = 0.41) (Table S3).

Conversely, solid precipitates from experiments supplemented with silica contained higher proportions of Fe(II) relative to the total measured iron, expressed in the ratio of $Fe(II)/FeT_{solid}$. All solids bioreduced in the presence of amended Si contained higher $Fe(II)/FeT_{solid}$ than the solids produced by the parallel experiments without added silica. Siliceous experimental products averaged 0.14 higher $Fe(II)/FeT_{solid}$ than solids formed without amended Si (Figure 1b, Table S3). The magnesium-augmented and AAS-only silica-amended experiments demonstrated particularly elevated $Fe(II)/FeT_{solid}$ (0.87 and 0.74) in precipitates compared to the solids in their silica-deficient counterpart experiments ($Fe(II)/FeT_{solid}$ = 0.69 and 0.53; Table S3).

The $Fe(II)_{aq}$ in abiotic control solutions ranged from 0.02 to 0.03 mM (Table S3), similar to the baseline levels of ferrous iron

observed by Reddy et al. (2016). In these control solutions, $Fe(II)_{aq}$ concentrations in the final solutions did not vary in the presence or absence of silica.

The calculated saturation indices of the various experimental set-ups indicated that a few phases were supersaturated under several conditions (Table S4). No mineral was at or above saturation (i.e., an SI ≥ 0) in the basal AAS media, in the AAS control final timepoint, or the magnesium-augmented media at the onset of the experiments. However, solutions with calcium were oversaturated with respect to aragonite and calcite even at the initiation of experiments, with supersaturation only increasing over the duration of the DIR and control experiments with rising pH. Other carbonate phases, including siderite and magnesite, were supersaturated in post-DIR experiments and in magnesium-amended experiments with added silica, respectively. While crystalline SiO_2 phases (chalcedony, cristobalite, and quartz) were also supersaturated in media amended with 1 mM silica, the amorphous SiO_2 phase that forms initially was undersaturated. Two silicate minerals were also supersaturated in silica-amended experiments. Greenalite was highly supersaturated in post-DIR experiments with added silica, while sepiolite, a magnesium silicate, was supersaturated in post-DIR and final control conditions with amended silica and magnesium.

3.2 | X-ray diffraction

Bulk XRD measurements on solids from *S. putrefaciens* incubations primarily produced either characteristic patterns of the calcium carbonate polymorphs, calcite and aragonite, or no definitive features (Figure S2). Diffractograms of both the AAS-only and magnesium-amended conditions, in the presence and absence of added silica, showed no detectable crystalline mineral phases. However, we identified the primary calcite peak (104) in the calcium-amended incubations, regardless of silica content. XRD profiles of incubations with added magnesium, calcium, and silica also demonstrated peaks indicative of both calcite and aragonite. Though we detected a possible magnetite diffraction peak (400) in the combined cation experiment with silica, no other diagnostic magnetite peaks were present in these measurements and the precipitates were unaffected by the proximity of a magnet. Oddly, XRD patterns from *S. putrefaciens* incubations supplemented with magnesium and calcium but with no added silica presented no discernable diffraction pattern, but this result could stem from the low quantity of material produced in this experiment or the composition of the subsample.

3.3 | Micro- to nanoscale characterization of experiments

We additionally investigated each incubation using electron microscopy and Raman spectroscopy techniques to fully characterize the nanocrystalline or amorphous nano- to microscale bioreduction mineral products.

3.3.1 | Abiotic control experiments

Control serum bottles without *S. putrefaciens* continued to contain ferrihydrite after >4 months (19 weeks) of incubation. TEM images and EDS mapping showed widespread iron- and oxygen-rich aggregates of ~5 nm rounded or blocky pseudohexagons characteristic of two-line ferrihydrite (2LFh, [Janney et al., 2000]) in samples without added silica (Figure S3A,B), with amended silica (Figure S3D,E), and with added silica, calcium, and magnesium (Figure S3G,H). HRTEM images and SAED demonstrated either amorphous precipitates by FFT (Figure S3E, inset) and/or precipitates composed of 2LFh based on the distinctive rings at 2.5 and 1.5 Å in an electron diffraction pattern (Figure S3G, inset). At the culmination of the control experiments with amended Si, STEM-EDS maps of the solids indicated substantial silica adsorption to ferrihydrite with an average of 8 at. % iron and 12 at. % silica in (Figure S3; Table S5A). We also detected low concentrations of silica in some EDS measurements of the AAS-only control solids (2–3 at. %) without amended Si (Figure S3, Table S5A).

Raman data showed Ca-carbonate polymorphs forming in calcium-bearing control experiments (Figure S4). We did not identify diagnostic carbonate spectral features in AAS-only and magnesium-bearing controls. However, Raman scans of calcium-augmented experiments indicated an abundance of calcite interspersed within the ferrihydrite. The addition of magnesium and calcium in controls with and without added silica produced both calcite and aragonite polymorphs.

3.3.2 | Artificial Archean Seawater (AAS, Calcium- and Magnesium-Free) incubations

AAS-only incubations of *S. putrefaciens* grown on ferrihydrite and lactate without added silica produced Fe-rich crusts intermixed with biomass or extracellular polymeric substances (EPS) after 19 weeks. SEM imaging revealed abundant spherical indentations across iron-rich crusts (Figure 2a,b), *S. putrefaciens* cells (see arrows in Figure 2b), and nanoscale globular chains and clusters of precipitates (Figure 2c; Table S5B). Microbial biofilms had high levels of adsorbed iron in these experiments (Table S5B), unlike the separated iron mineral precipitates that formed in the other cation-containing conditions.

Our TEM/STEM images also resolved cells with associated 50–100 nm lath-like phases and sulfur-containing granules (Figure 2d–g). We identified these laths as lepidocrocite, or γ-FeOOH, by their characteristic 6.23 Å spacing parallel to the elongated axis, 3.3 Å (210) spacing (Figure 2d,e) and their Fe content (Figure 2g; Table S5B). This lepidocrocite appeared intimately associated with either cell surfaces (Figure 2d) (similar to Glasauer et al., 2007; Glasauer et al., 2002) or an organic-rich matrix (Figure 2e). Additionally, we detected 50–60 nm granules composed mainly of sodium and sulfur (7 at. % Na, 4 at. % S, and <1 at. % Fe) (Table S5B) associated with the cellular membranes of AAS-only *S. putrefaciens* in HAADF images and TEM–EDS maps (Figure 2d,f). However, the AAS medium was absent of sulfur constituents and lacked sulfur-containing amino

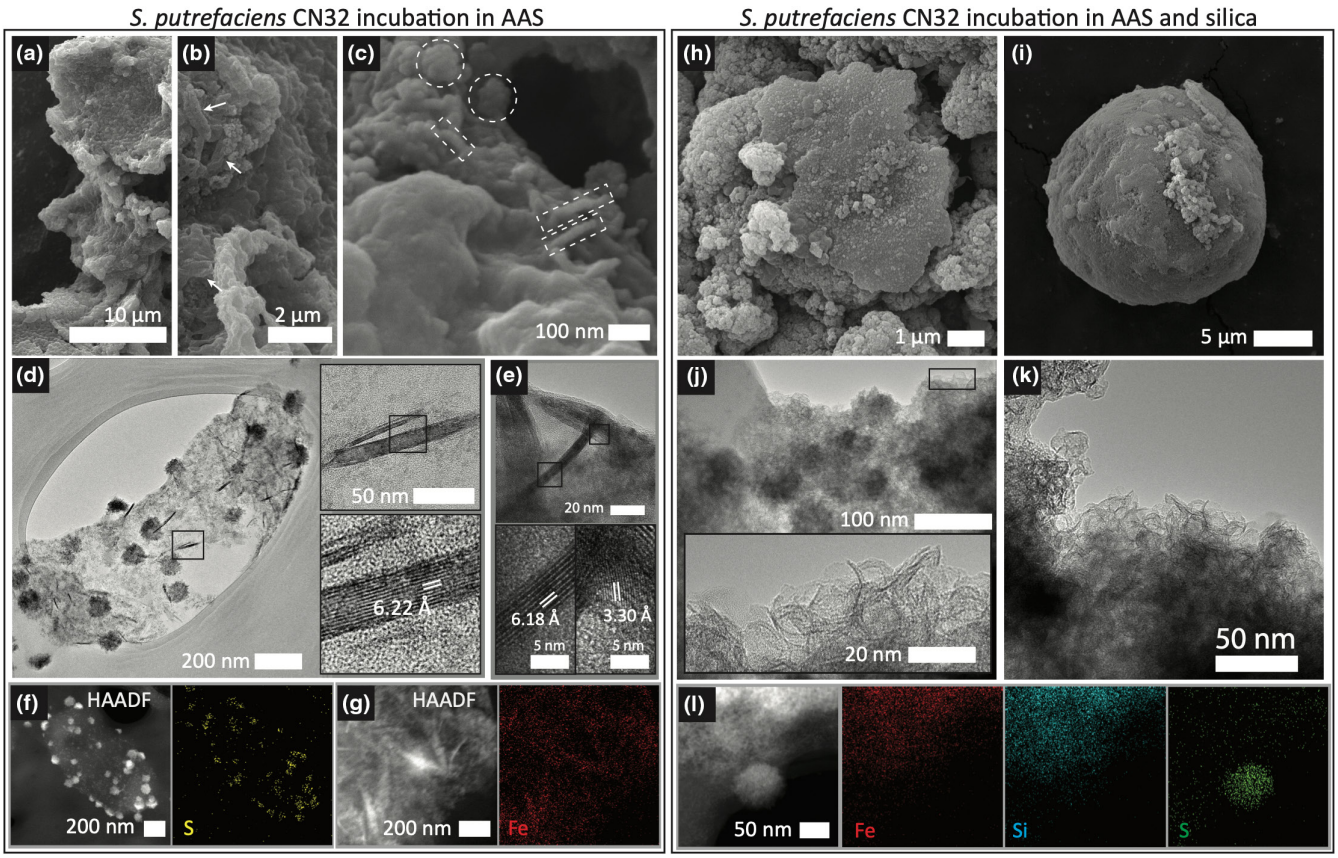

FIGURE 2 Electron imaging and elemental maps of biomineral precipitates from simple AAS media (calcium- and magnesium-free) experiments. Representative images revealed: (a) Cohesive iron crusts, (b) cells (denoted by arrows) entrained in an iron-rich matrix, and (c) nanometer-scale chains and clusters of globules (represented by dashed rectangles and circles, respectively); (d) *S. putrefaciens* cells with lepidocrocite (γ-FeOOH) laths embedded in the cellular membrane, shown at higher magnification (upper inset) and HRTEM showing laths with characteristic 6.2 Å interplanar spacing of lepidocrocite (lower inset); (e) Elongated laths of γ-FeOOH in an organic film with typical 6.2 and 3.3 Å spacing; STEM-HAADF and corresponding EDS mapping of membrane-associated granules showing S in yellow (f) and membrane-bound lepidocrocite, with Fe shown in red (g). In silica-amended experiments, observations included: (h) SEM images of irregular crusts and (i) spherical morphologies; (j) TEM images of amorphous, wavy precipitates intermixed with darker globular structures; higher magnification images reveal the sheet-like morphologies of the wavy structures (j, inset) and homogeneity of the particles (k); (l) STEM-EDS mapping of a similar/neighboring area shows an Fe (red) and Si (cyan) rich matrix with an associated sulfur-rich granule (green).

acids that could be sources of sulfur (only containing arginine, glutamine, and serine). We suspect this sulfur derived from cellular stores of residual sulfur-rich compounds from the rinsed stock cultures grown in TSB.

AAS-only incubations augmented with silica generated similar iron-rich crusts (Figure 2h) and larger-scale (~10 µm) spherical aggregates (Figure 2i). TEM analyses revealed this experimental condition produced a silica- and iron-rich coprecipitate matrix, composed of thin, platy particles lacking diffracting domains or identifiable fringes (Figure 2j–l). The curling, poorly layered structures of this Fe–Si phase (Figure 2j,k) were distinct from the control precipitates that instead contained pseudohexagonal crystallites of 2LFh (Figure S3D–F). These siliceous AAS-only precipitates also contained 40–60 nm sulfur-rich granules similar to their silica-free counterparts; however, the sulfur grains, perceptible as dark, round features in Figure 2j, were interspersed throughout the iron- and silica-rich precipitates (Figure 2l) and lacked clear associations with cell surfaces.

3.3.3 | Calcium-augmented incubations

Supplemented with calcium, *S. putrefaciens* CN32 incubations produced large (10–50 µm) calcium carbonate minerals and iron oxyhydroxide minerals (Figure 3). In experiments with calcium but lacking added silica, we observed the precipitation of abundant calcium carbonate minerals. SEM images demonstrated the broad variety of Ca-carbonate minerals and morphologies, from stacks of blocky calcite with acicular aragonite overgrowths (Figure 3a) to large rhombohedral crystals featuring irregular surfaces (Figure 3b). However, we found no evidence of iron-rich carbonates such as ankerite or siderite in these experiments. The carbonate crystals contained <5% Fe by EDS (e.g., Table S5C), and we did not detect diffraction patterns or Raman spectra diagnostic of siderite or ankerite in the precipitates using SAED, XRD, and Raman spectroscopy.

We also observed abundant clusters of iron-rich rods that aggregated into globular forms (Figure 3c). SEM–EDS maps highlighted

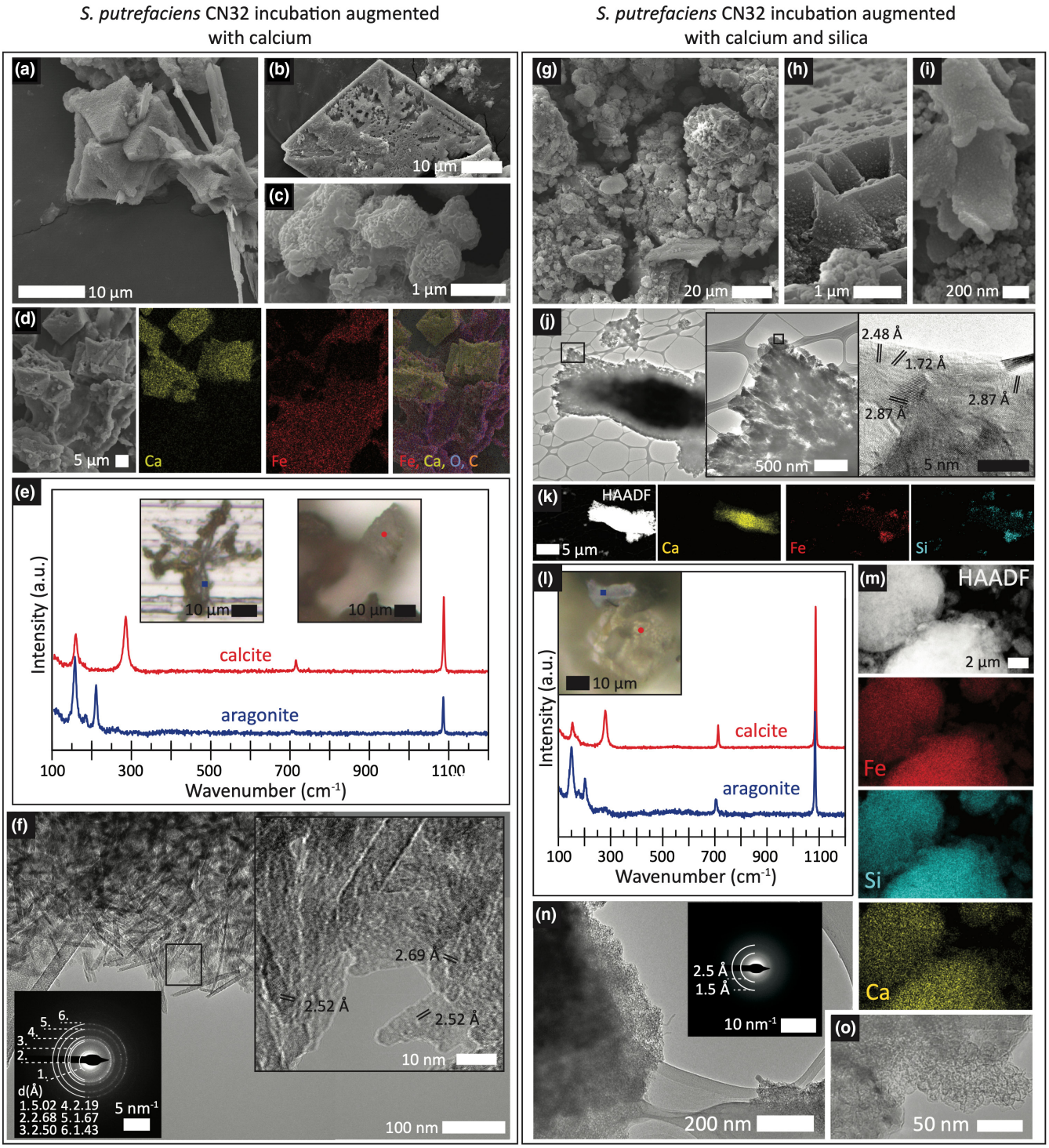

FIGURE 3 Characterization of biominerals formed in *S. putrefaciens* incubations amended with calcium. Representative data included: from experiments lacking added silica, (a, b) SEM images of calcium carbonate minerals and (c) aggregates of rod-shaped iron-rich precipitates, with (d) elemental maps showing biomineral precipitates composed of calcium (yellow), iron (red), oxygen (blue), and carbon (orange); (e) Raman spectra of calcite (red) and aragonite (blue) minerals paired with corresponding images demarcating scan locations; (f) TEM image of needle morphologies with SAED inset showing reflections characteristic of goethite, and HRTEM and FFT insets of demarcated region with lattice fringes also corresponding to α-FeOOH. In experiments with added silica; (g-i) SEM images of abundant carbonates comingled with Fe–Si coprecipitates; (j) TEM image of a bundle of calcium carbonate minerals, at higher magnification (black rectangle, inset) and HRTEM of polycrystalline edge showing nanodomains of aragonite; (k) STEM-HAADF and corresponding EDS maps of the bundle of carbonate crystallites imaged in (j) showing the elemental distribution of calcium (yellow), iron (red), and silica (cyan); (l) Raman spectra of calcite (red) and aragonite (blue) minerals paired with corresponding images of scan locations; (m) disc-like aggregates of iron- and silica-rich coprecipitates; (n) TEM image of Fe–Si aggregates with inset SAED presenting mainly amorphous phases and some residual 2LFh; (o) HRTEM image of Fe–Si coprecipitates exhibiting curled sheet-like structures.

the separation between iron and calcium carbonate phases, with distinct carbonate crystals forming alongside iron-rich precipitates (Figure 3d; Table S5C). Raman analysis of spindle-like and euhedral carbonate minerals in calcium-amended experiments produced distinctive spectral features of both aragonite and calcite polymorphs (Figure 3e), validating the identification of calcium-rich particles evident in SEM imaging. TEM-based imaging and analyses of the iron-rich precipitates revealed aggregates of 10–20 nm acicular needles (Figure 3f). The SAED pattern of these needles showed strong reflections for goethite (Figure 3f inset, Table S6). The 2.50 and 2.68 Å d-values obtained from FFT of the lattice fringe of individual needles (Figure 3f inset) were also consistent with the (001) and (102) planes of goethite.

Silica-supplemented and calcium-bearing incubations yielded abundant calcium carbonate precipitates immersed in a siliceous iron matrix (Figure 3g, Table S5C). Calcite euhedra presented step defects (Figure 3h). Both carbonate and iron minerals commonly displayed a veneer of nanocolloids (Figure 3h,i). Similarly, TEM imaging and analysis showed a dense bundle of crystallites (Figure 3j) enriched in calcium associated with aggregates of iron and silica (Figure 3k). FFT of the HRTEM image of these nanocrystallites (Figure 3j right inset) exhibited nanometer-scale domains consistent with the (002), (102), and (023) planes of aragonite (Table S6). Raman measurements of precipitates harvested from these *S. putrefaciens* incubations indicated an abundance of both calcite and aragonite (Figure 3l). In several instances, we observed orange-tinted calcite minerals alongside pristine, unaltered aragonite in optical micrographs collected during Raman analysis (Figure 3l inset).

In these incubations with calcium and silica, we also identified amorphous, wavy iron- and silica-rich precipitates by TEM imaging. Aggregates of Fe–Si coprecipitates formed rounded morphologies in HAADF images (Figure 3m). These aggregates were low in calcium (1 at. %), but high in silica (24 at. %) and iron (19 at. %) (Figure 3m; Table S5C). An SAED pattern of this siliceous deposit showed faint characteristic reflections of 2LFh, suggesting the amorphous wavy precipitates were intermixed with some residual ferrihydrite from the starting substrate (Figure 3n). The morphologies of these Fe–Si precipitates were similar to the AAS-only experiment, displaying curling sheet-like structures (Figure 3o).

3.3.4 | Magnesium-augmented incubations

In incubations of *S. putrefaciens* supplemented with magnesium but without amended silica, we observed the precipitation of iron-rich nanogranules and rods with occasional plate-like minerals. SEM and TEM images show minerals suspended in a webbing of EPS stretched across the lacey Formvar support of the TEM grid (Figure 4a) as well as cells embedded in aggregates of precipitates (Figure 4b, arrows). We hypothesize that biomass provided a matrix for iron-rich minerals, such as secondary FeOOH and possibly remnant or recrystallized ferrihydrite. TEM imaging of these iron crusts revealed aggregates of rod-shaped particles (Figure 4c) containing a high percentage of Fe (18 at. %) and limited magnesium incorporation (<1 at. %) (Figure 4d; Table S5D). HRTEM of these particles showed rods with sub-angular facets (Figure 4c), unlike the acicular goethite needles identified in calcium-amended experiments (Figure 3f). Crystallites yielded diffraction characteristics, which could indicate a mixture of several iron (oxyhydr)oxide minerals. SAED reflections with *d*-values that correspond closely to both six-line ferrihydrite (6LFh) and goethite suggest a possible a mixture of these phases (Figure 4c; Table S6). Additionally, FFT collected from HRTEM of the blunted rods exhibited spacing characteristic of the (012) plane of hematite (3.68 Å) (Figure 4c, inset; Table S6). Hence, the sub-angular morphology combined with the hazy, smeared reflections of this aggregate (Figure 4c, SAED inset), in lieu of the more discrete polycrystalline reflections of goethite visible in Figure 3f, could suggest a mixture of poorly crystalline 6LFh, goethite, and hematite in this set of experiments.

In incubations amended with magnesium and silica, large cohesive masses of iron- and silica-rich granules dominated bioreduced precipitates. We observed 5–10 μm globular structures intermixed with unstructured crusts and planar deposits with SEM (Figure 4e). TEM imaging revealed micron-scale homogeneous aggregates composed of thin, curling particles (Figure 4f), similar to the Fe–Si precipitates in siliceous AAS-only and calcium-amended experiments. An SAED pattern of a large sheet of these phases also contained diffuse reflections of 2LFh (1.5 and 2.5 Å) (Figure 4f inset), suggesting that the wavy structures develop in association with the 2LFh substrate. HRTEM imaging underscored the stacked, curling forms of these fragile, folded structures (Figure 4g), while FFT indicated an amorphous composition of these wavy phases (Figure 4g, inset). STEM-EDS spectra and STEM mapping indicated that the structures consisted of approximately 24 at. % Si, 27 at. % Fe, and 2 at. % Mg (Figure 4h; Table S5D). HAADF images and STEM-EDS also revealed rare hexagonal phases with similar atomic percentages relative to the surrounding matrix of folded precipitates (Figure 4h). However, thick layers of overlying Fe–Si aggregates possibly masked elemental distinctions in HAADF images and/or inhibited identification of the sparse hexagonal inclusions by electron diffraction.

Additionally, STEM-EDS mapping showed *S. putrefaciens* membranes enriched in sulfur (6 at. %) (Figure S5B; Table S5D). In contrast to the sulfur-rich granules associated with the cellular membranes of AAS-only *S. putrefaciens* (Figure 2d,f; Figure S5A), sulfur was instead uniformly distributed across cell membranes in the magnesium-amended incubation (Figure S5B).

3.3.5 | Calcium- and magnesium-augmented incubations

In silica-free *S. putrefaciens* incubations supplemented with both calcium and magnesium, we observed 5–50 μm calcium carbonate precipitates alongside well-defined, nanobotryoidal iron-rich clusters (Figure 5a,b). These experiments yielded a broad range of carbonate

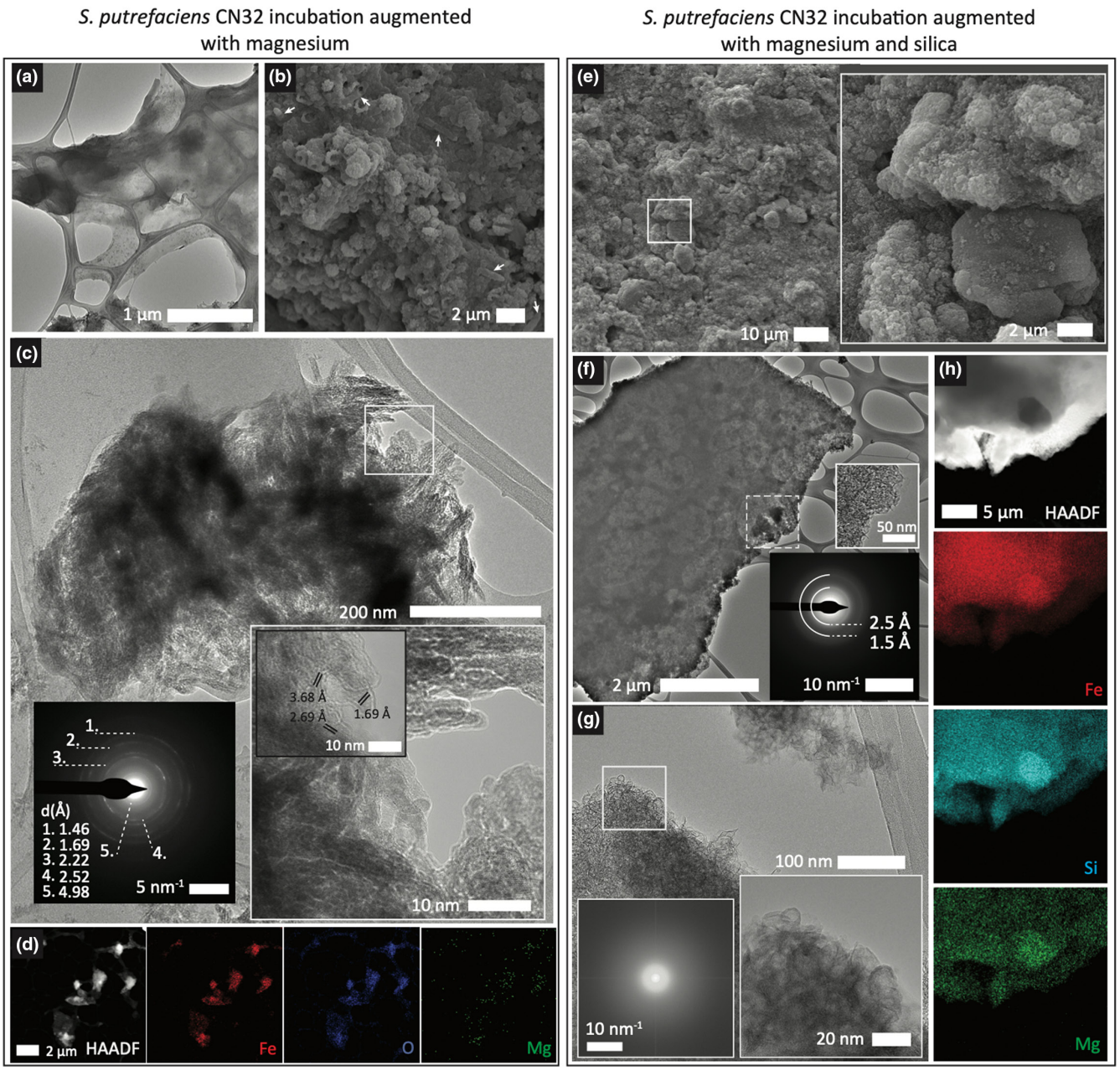

FIGURE 4 Images and analysis of biominerals formed in *S. putrefaciens* incubations amended with magnesium. Representative observations include: from incubations without added silica, (a) TEM images of a webbed network of organic-precipitate mixture; (b) SEM images of biomass-mineral assemblage containing granular iron crusts and entrained cells (denoted by white arrows); (c) TEM of blunt, rod-shaped minerals with SAED (inset) of whole region showing reflections characteristic of goethite, 6LFh, and possibly hematite, with HRTEM (of white rectangle) and SAED of overlapping rounded rods as insets; (d) STEM-EDS maps of rod aggregates with iron, oxygen, and magnesium shown in red, blue, and green, respectively. From silica-amended experiments, (e) SEM images Fe–Si precipitates with some platy morphologies at higher resolution as inset; (f) TEM image of Fe–Si aggregates with inset SAED showing faint 2LFh reflections and zoom-in inset showing thin wavy structures; (h) STEM-EDS analysis similar Fe–Si rich-precipitates, showing iron (red), silica (cyan), and magnesium (green); and (g) TEM imaging of Fe–Si coprecipitates showing folding, curling phases, with HRTEM and FFT insets revealing amorphous structures.

mineral morphology, as shown in Figure 5a–c. Using Raman microspectroscopy, we identified these phases as both calcite and aragonite (Figure 5c), calcium carbonate polymorphs that were undetected by XRD measurements (Figure S2). TEM imaging of smaller precipitates revealed nanoscale iron-rich rods (Figure 5d,e). Electron diffraction patterns of these rods showed reflections corresponding to goethite (Figure 5d), and lattice fringes from FFT of HRTEM of these rods (4.19, 2.53, and 1.76 Å) consistent with the (101), (011), and (112) planes of goethite (Figure 5d, inset). In agreement with this identification, TEM–EDS maps also showed minerals rich in iron (26 at. %) and oxygen but depleted in both calcium and magnesium (<1 at. %) (Figure 5e; Table S5E).

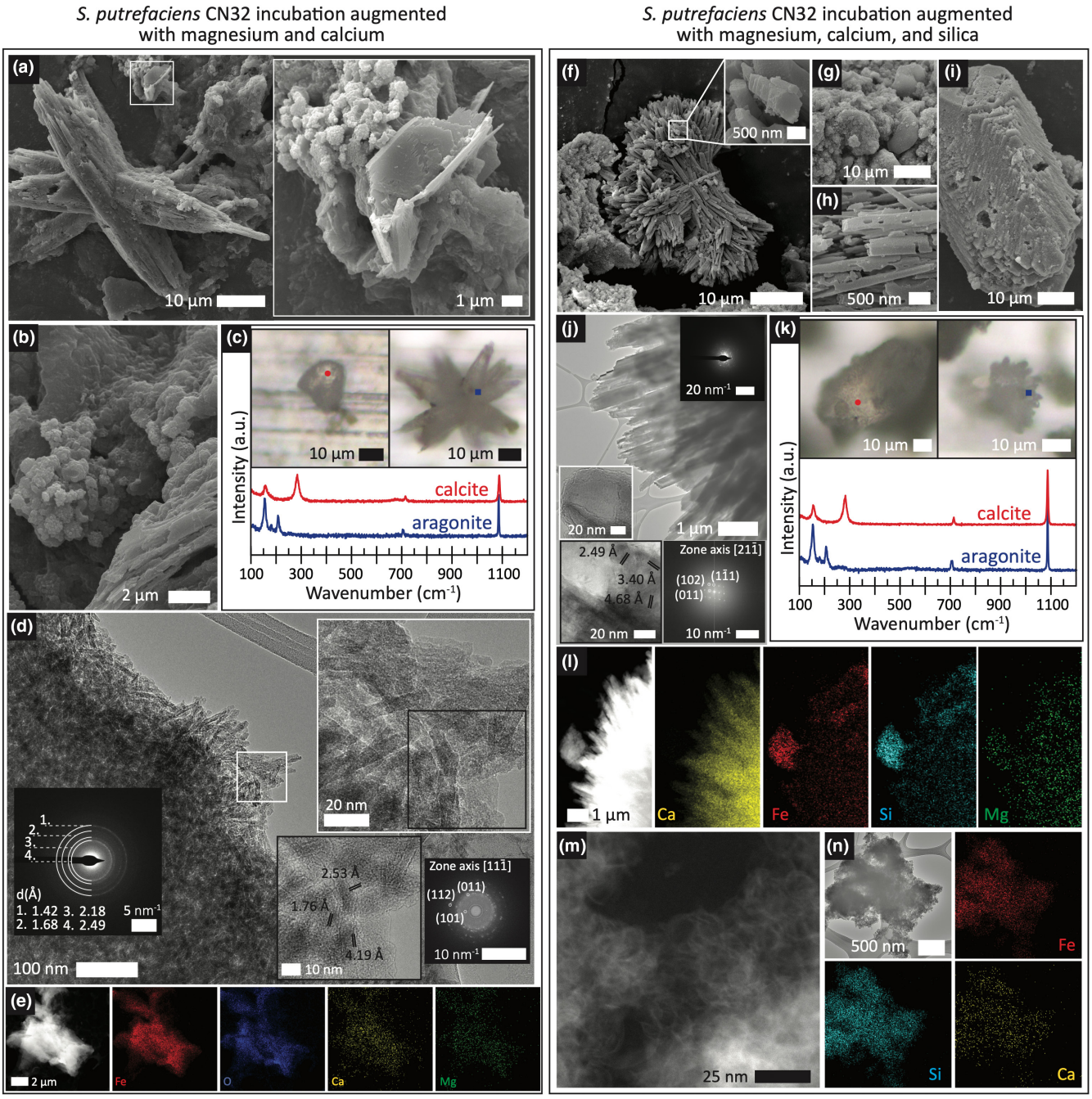

FIGURE 5 Characterization of biominerals formed in *S. putrefaciens* incubations amended with calcium and magnesium. Observations of products from incubations without added silica include: (a) crystalline carbonates imaged by SEM and (b) spherical crust-like phases; (c) Raman measurements of different carbonate morphologies indicating calcite and aragonite minerals; (d) TEM images of aggregates of rod-like phases and SAED suggesting goethite, with HRTEM and FFT (insets) also indicating d-values consistent with goethite; (e) STEM-EDS mapping of iron-rich masses depicting iron, oxygen, calcium, and magnesium in red, blue, yellow, and green, respectively. In experiments with silica present: SEM imaging shows acicular (f) and blocky (g) morphologies, perforated blades (h), and stacked rhombohedral crystals (i); (j) TEM images show a cluster of acicular crystals with inset SAED showing polycrystalline reflections, and HRTEM and FFT indicating crystals with *d*-values consistent with aragonite (lower inset); (k) Raman measurements confirm the presence of calcite and aragonite polymorphs; (l) STEM-EDS mapping showing the distribution of calcium (yellow), iron (red), silica (cyan), and magnesium (green) in the Ca- and Fe-rich precipitates; (m) HAADF image indicating the forms of the wavy, friable phases; and (n) STEM-EDS mapping of precipitates with iron (red), silica (cyan), and calcium (yellow).

In the presence of silica, the magnesium- and calcium-amended *S. putrefaciens* incubation produced even more complex carbonate morphologies. We detected 30–40µm calcium carbonate polymorphs, with <1 at.% incorporation of magnesium or iron, manifesting as bundles of outgrowing acicular needles branching out of a central plane (Figure 5f), globular forms embedded in a siliceous

matrix (Figure 5g), blunt-edged porous blades dusted with silica-rich nanocolloids (Figure 5h), and rhombohedral calcium carbonate crystals (Figure 5i). SAED of the outgrowing blades showed a complex, polycrystalline pattern (Figure 5j). HRTEM of an edge of one acicular needle (Figure 5j, inset) analyzed by FFT showed d-values (2.49, 3.40, and 4.68 Å), with an interplane angle of 76°, consistent with the (011), (111), and (102) planes of aragonite (Figure 5j, lower subset). Raman analyses confirmed that these carbonate minerals were both aragonite and calcite (Figure 5k), a finding also supported by bulk XRD analysis (Figure S2). Additionally, TEM imaging showed a distinct separation of the carbonate crystals from iron- and silica-rich phases (Figure 5l). High-magnification HAADF imaging of these aggregates indicated the platy, curling morphology of the nanostructures (Figure 5m), rich in iron and silica (Figure 5n), and comparable to the friable Fe–Si precipitates that formed in other silica-augmented bioreduced experiments.

4 | DISCUSSION

Overall, these experiments testing microbial iron reduction in silica-rich simulated Archean marine environments produced several secondary mineral products. Depending on whether silica, calcium, and/or magnesium was added to the experimental medium, we observed secondary ferric oxyhydroxides, such as goethite and lepidocrocite, and other precipitates including calcium carbonate polymorphs and proto-iron silicates (Figure 6). We explore these products and hypothesize how they formed below.

4.1 | Secondary mineral products from DIR

4.1.1 | Proto-iron silicates

We observed the formation of novel Fe(II)-rich iron-silica coprecipitates in our experimental incubations inoculated with *S. putrefaciens*. In tandem, our Ferrozine and silicomolybdate assay results suggest that silica sequesters ferrous iron into iron-silica solid phases. In experiments without amended silica, biogenic $Fe(II)_{aq}$ increased in solution, while this Fe(II) predominantly partitioned into solid precipitates under siliceous conditions (Figure 1a,b, Table S3). In silica-containing experiments, the average $Fe(II)/FeT_{solid}$ was approximately 25% higher than those in experiments without added dissolved silica (Table S3). The incorporation of biogenic ferrous iron and dissolved silica into newly formed iron-silica coprecipitates could explain the depletion of $Fe(II)_{aq}$ and Si_{aq} in the silica-amended solutions. Silica-amended experiments without added divalent cations or solely with added magnesium contained both negligible (<0.1 mM) final $Fe(II)_{aq}$ and large decreases in Si_{aq}, with approximately 40%–50% of the starting Si removed from solution (Figure 1c; Table S2). These AAS and Mg-amended experiments additionally had the highest $Fe(II)/FeT_{solid}$ ratios, as the magnesium-amended solutions generated solids with 74% Fe(II) and the simple AAS solutions formed solids with 87% Fe(II) (Figure 1a,b, Table S3). However, the addition of Ca^{2+} distinctly altered the distribution of ferrous iron in silica-amended experiments, increasing $[Fe(II)_{aq}]$ to 0.24–0.3 mM and lowering

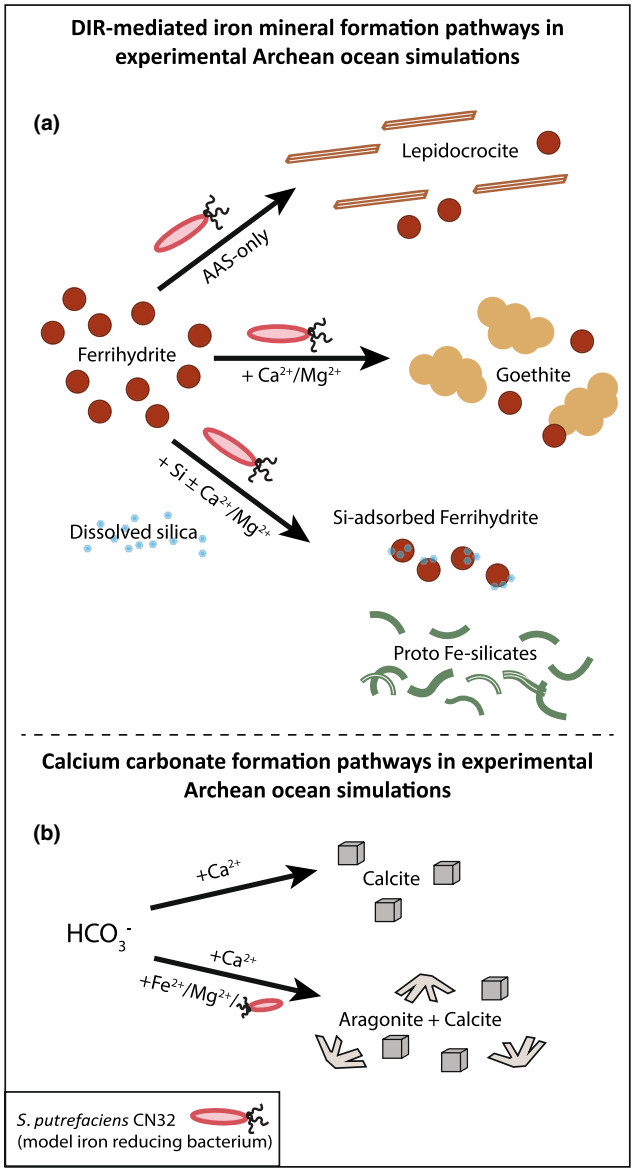

FIGURE 6 Summary of mineral formation pathways observed in our experimental simulations of Archean marine environments testing the effects of dissolved Si, Ca^{2+}, and Mg^{2+} on the secondary products of DIR. (a) Pathways of iron mineral formation showed a dependence on the dissolved ions, with the basal AAS media (without added Si, Ca^{2+}, and Mg^{2+}) forming lepidocrocite, γ-FeOOH, upon DIR (top arrow); the addition of Ca^{2+} and/or Mg^{2+} resulting in the formation of goethite, α-FeOOH, after DIR (middle arrow); and the addition of Si with or without Ca^{2+} and/or Mg^{2+} generating proto-iron silicates upon DIR (bottom arrow). (b) Calcium carbonate precipitation was also observed, with calcite forming in the presence of added Ca^{2+} (top arrow) while calcite and aragonite both precipitated in the presence of added Ca^{2+} when Mg^{2+} was present, or when Fe^{2+} was present as a result of DIR, and/or when organics were released by *S. putrefaciens*.

$Fe(II)/FeT_{solid}$ ratios (Figure 1a,b, Table S3), which we explore further below. In all experimental conditions without added silica, substantially more (0.1–0.5 mM) $Fe(II)_{aq}$ accumulated in solution, consistent with the formation of Fe(II)-rich siliceous phases in silica-amended experiments.

Indeed, in incubations amended with dissolved silica, micro- and nano-scale imaging revealed the formation of novel iron-silica coprecipitates. The elevated $Fe(II)/FeT_{solid}$ in silica-amended precipitation products could point to the formation of mixed-valence Fe-oxides like magnetite, but we did not detect magnetite under these conditions by SEM- or TEM-based analyses, Raman spectroscopy, XRD, or magnetic reaction. Instead, we observed the formation of abundant, light gray, wispy precipitates over time (Figure S6). In our electron microscopy imaging and analyses, extensive Fe–Si clusters of amorphous curling structures were present in all silica-bearing bioreduction conditions (e.g., Figures 2j–l, 3m–o, 4f–h and 5l–n) but absent in control experiments. These iron- and silica-rich precipitates lack definitive crystal structure, including any resolvable lattice fringe in HRTEM imaging. Though SAED patterns suggest some iron-silica precipitates contain a component of 2LFh, the coprecipitates are morphologically distinct from their antecedent ferrihydrite minerals, which are composed of pseudohexagonal crystallites (Figure S3). The iron-silica phase is instead characterized by thin, curling, and folding layers (e.g., Figure 2j), as well as high Fe, Si, and O (Table S5B–E). Furthermore, the higher $Fe(II)/FeT_{solid}$ of the silica-amended solids compared to bioreduced solids without added silica implies that these curled silica-rich phases are Fe(II)-rich. Therefore, we suggest that these structures are incipient Fe(II)-rich proto-silicates (Figure 6a).

We hypothesize that the precipitation of Fe(II)-rich phases is promoted by cell-mineral interactions resulting in biomass-mineral aggregates that retain and adsorb local ferrous iron. The surface properties of *S. putrefaciens* have been observed to enhance aggregation of ferrihydrite particles and cells, forming packed structures (Glasauer et al., 2001; Zachara et al., 2002; Zegeye et al., 2010). These cell-mineral aggregates create microenvironments with elevated pH and higher concentrations of metabolic byproducts, like Fe(II) and CO_3^{2-} (Pallud et al., 2010; Roden & Urrutia, 2002; Zachara et al., 2002; Zegeye et al., 2010). For example, Zegeye et al. (2010) reported the highest retention of ferrous iron in dense microbe-mineral aggregates of *S. putrefaciens* and γ-FeOOH, and these Fe(II)-rich microenvironments led to the formation of a more reduced product, green rust, rather than magnetite. Similarly, Pallud et al. (2010) observed that sand-ferrihydrite aggregates inoculated with *S. putrefaciens* produced secondary minerals, including goethite/lepidocrocite and siderite, within the inner fractions of aggregates, while outer portions showed limited secondary iron phases. Indeed, the *S. putrefaciens* biofilm-mineral aggregates that developed in our AAS-only experiments—and more extensively in the silica-amended condition—appeared to sequester Fe(II), as indicated by our EDS observations of high Fe in AAS biomass, very low $Fe(II)_{aq}$ in the final media solutions, and high $Fe(II)/FeT_{solid}$ in the precipitate-biomass solid pellet (Figures 1a,b and 2a–c,g, Tables S3 and S5B).

We further posit that ferrihydrite-adsorbed silica and ferrous iron promoted the precipitation of iron-silica coprecipitates in these experiments. SAED patterns of the iron-silica coprecipitates in our biotic experiments showed weak ferrihydrite reflections (Figures 3n and 4f). Not only are ferric hydroxides highly adsorptive of Si, but ferrihydrite surfaces also act as templates for silica polymerization at pH 6–8.5 (Swedlund & Webster, 1999), potentially facilitating the formation of Fe–Si precipitates. Siliceous conditions could also enhance the aggregation of clustered microbial biomass, silica, and FeOOH minerals. Zachara et al. (2002) noted that, at circumneutral pH, the ferrihydrite surface favors the strong sorption of silicic acid and Fe^{2+}, and upon Fe(III) respiration, these adsorbed ions are concentrated in the microenvironments within the aggregated ferrihydrite-biomass clusters. These ions and reaction products may then react to form aqueous complexes and ultimately new solid phases. Therefore, biomass-ferrihydrite aggregates in our experiments may have produced microenvironments with increased concentrations of Si and Fe^{2+}, as well as templating ferrihydrite surfaces, stimulating the precipitation of iron-silica phases.

The inclusion of calcium in the experimental medium likely resulted in differences in these localized microenvironments. The presence of calcium appeared to produce much higher final $Fe(II)_{aq}$ and lower $Fe(II)/FeT_{solid}$ ratios, potentially associated with tendency of calcium to disaggregate microbe-mineral aggregates and outcompete Fe^{2+} adsorption on ferrihydrite surfaces. We observed the highest concentrations of $Fe(II)_{aq}$ in experiments without added silica but with 10 mM Ca^{2+}, a trend that increased with the addition of magnesium (Table S3). Even in calcium-bearing experiments amended with silica, we identified substantially higher $Fe(II)_{aq}$ compared to calcium-lacking experiments (Figure 1a,b, Table S3). A previous study found that multicellular aggregates of *Shewanella oneidensis* MR1 cultures did not form or disaggregated in the presence of even low Ca levels (0.68 mM Ca^{2+}) under anaerobic growth conditions (McLean et al., 2008). If calcium similarly limited cell-ferrihydrite aggregation in our anaerobic Fe(III) respiration experiments, this would likely allow more bio-generated Fe(II) to escape into solution while increasing the exposed surface area of ferrihydrite particles to bioreduction and Si adsorption. Additionally, Ca^{2+} is used to dislodge weakly adsorbed divalent ions, including Fe^{2+}, from ferrihydrite surfaces (Cismasu et al., 2013; Kinsela et al., 2016). In calcium-amended experiments, calcium would thus be expected to decrease the retention of Fe(II) in ferrihydrite-associated complexes, as well as inhibit the formation of microbe-mineral aggregates.

Previous abiotic experiments formed proto-Fe(II) silicates in Archean-like conditions when pH was elevated to ≥7.5 (Hinz et al., 2021; Tosca et al., 2016). Microbial iron respiration increases alkalinity and drives pH to these higher values, exceeding pH 7 (e.g., Bergmann et al., 2013). While pH values of ≥7.5 are higher than the predicted pH of the Archean ocean, DIR increased the bulk pH in our experiments (Table S1) and potentially created even higher-pH microenvironments in microbe-mineral aggregates. Thus, the increasing shift in pH could have made the precipitation of proto-iron silicates more favorable in our experimental set-up. In the presence

of Ca^{2+}, the experiments concluded with lower pH (<7.5), likely due to the formation of calcium carbonate minerals. The lower pH and extensive precipitation of calcium carbonate minerals may have contributed to the heightened $Fe(II)_{aq}$ and Si_{aq} of the combined Ca^{2+}- and Mg^{2+}-amended experiments, potentially limiting–but not preventing–the formation of proto-iron silicates.

Because the iron-silica curling precipitates were absent in silica-amended control products, we further propose that Fe(II) was essential to the formation of these phases. Our abiotic control experiments solely contained ferrihydrite and calcium carbonate phases after over the >4.5 month incubations (Figures S3 and S4). Conversely, experiments with *S. putrefaciens* performing Fe(III) respiration and producing Fe(II) in the presence of dissolved silica invariably resulted in proto-iron silicate phases, regardless of whether Ca^{2+} or Mg^{2+} were in the solution. Our findings support the Harder (1978) hypothesis that Fe(II) plays a critical role in the formation of proto-iron silicates under environmentally relevant conditions (i.e., <2 mM Fe and Si). With iron introduced solely as ferrihydrite, we found that the biogenic production of Fe(II) from DIR was required to produce these precursor iron silicates.

4.1.2 | Carbonates

The most evident effect of adding calcium was in the production of calcium carbonate polymorphs (Figure 6b), which formed in both *S. putrefaciens* incubations and control experiments (see Figure S4). Both aragonite and calcite were slightly supersaturated in the starting solutions, with the initial saturation index (SI) of each phase beginning at $SI_{Calcite}$ of 0.16–0.28 and $SI_{Aragonite}$ of 0.017–0.13 in experiments with either Ca^{2+}-only or both Ca^{2+} and Mg^{2+} (Table S4). Over the course of the experiments, as pH increased either due to the DIR reaction, CO_2 exsolution in the N_2 headspace, and/or the higher-pH buffering of the sodium metasilicate Si source, these SI values would have increased. Indeed, at the final pH of 7.5–7.6 in the post-DIR experiments, the $SI_{Calcite}$ increased to ~0.6–0.8 while $SI_{Aragonite}$ increases to ~0.4–0.65, again with either Ca-bearing chemistry. Our observation of aragonite, despite being thermodynamically unfavorable relative to calcite, is likely due to the favorable precipitation of aragonite in the presence of Fe(II) and Mg(II) (Berner, 1975; Mucci & Morse, 1982; Zeller & Wray, 1956). Fe(II) inhibits normal calcite spiral growth (Di Lorenzo et al., 2017) and the incorporation of Mg(II) into the calcite lattice inhibits crystal growth either by increasing surface energy (Sun, Jayaraman, et al., 2015) or increasing calcite solubility (Davis et al., 2000).

However, we observed both aragonite and calcite polymorphs in *S. putrefaciens* incubations amended with calcium, under conditions both with and without magnesium. This dual finding signals the intricacies of polymorph formation in biological solutions. Although the iron-reducing environment and supplemented magnesium would suggest aragonite precipitation, the [Mg]/[Ca] ratio in our experiments (initially at 1 where both present) remained lower than the critical limit established for aragonite selection (i.e., [Mg]/[Ca] ≥ 2; (Sun, Jayaraman, et al., 2015)), potentially enabling the formation of both polymorphs across local heterogeneity. In calcium-amended conditions with *S. putrefaciens*, initial calcite precipitation was likely overtaken by aragonite mineralization due to the increasing ferrous iron inhibiting calcite (Dromgoole & Walter, 1990; Meyer, 1984) and/or the development of an EPS matrix (Lyu et al., 2020). In contrast, we identified only calcite and no aragonite in Raman scans of minerals in Ca-amended abiotic controls (Figure S4), confirming the role of cellular organics, biogenic Fe(II), and Mg^{2+} in promoting aragonite precipitation under the other experimental conditions.

Dissolved silica could also play a role in carbonate crystal growth or polymorphism in the bioreduction incubations with *S. putrefaciens*. Kellermeier et al. (2013) observed both the stabilizing effects of surface-adsorbed silica on metastable $CaCO_3$ polymorphs and silica-enhanced calcite growth at low temperatures. Unlike silica-free experiments that contained large, more singular calcium carbonate crystals, we frequently observed smaller individual needles and blades fusing into larger mineral aggregates in Si-amended experiments (e.g., Figure 5f,h); however, the exact role of dissolved silica in carbonate morphology is difficult to quantify in these limited experiments.

Iron carbonates, including siderite, were not detected in our experimental conditions, which we attribute to the low concentrations of $Fe(II)_{aq}$ and the large divergence in the growth kinetics between calcite and siderite. Our experiments started with 1.5 mM Fe(III) in ferrihydrite and 10 mM HCO_3^-, evolving to a final measured solution chemistry with a ~1:20 ratio of aqueous $Fe(II)_{aq}$ to calcium or magnesium (where $[Fe(II)_{aq}] \leq$ ~500 μM and initial [Ca] and [Mg] was 10 mM). Siderite saturation was maximized in DIR experiments with combined Ca and Mg but without Si, where $Fe(II)_{aq}$ reached 500 μM at the final pH of 7.5; under these conditions, $SI_{siderite} = 1.7$ while $SI_{calcite} = 0.7$. At environmental conditions of 25°C and 1 atm, when both siderite and calcite are supersaturated, the growth rate of calcite is approximately seven orders of magnitude faster than that of siderite, a behavior likely explained by the smaller ionic radius of Fe^{2+} and requisite higher activation energy to form siderite (Jiang & Tosca, 2020). More importantly, siderite precipitation proceeds through an amorphous ferrous carbonate [AFC: $Fe(CO_3)_{0.5}OH$] precursor, which requires a higher supersaturation threshold than obtained by our experiments. The threshold for AFC precipitation is an $SI_{siderite} >$ ~2.8 (Jiang & Tosca, 2019), and our final solution chemistry remained below this minimum. In contrast, the supersaturation required for aragonite and calcite precipitation (Busenberg & Plummer, 1986) were surpassed in all our Ca-bearing solutions. Therefore, based on kinetic considerations, we would expect calcium carbonates to precipitate instead of iron-rich carbonates in this experimental set-up. Our experimental chemistry was distinct from a previous set of experiments simulating BIF bioreduction where *Shewanella oneidensis* MR-1 cultures reduced 5 mM ferric hydroxides to >3 mM $Fe(II)_{aq}$ in solutions with 0–10 mM Ca^{2+} and 0–100 mM Mg^{2+} (Zeng

& Tice, 2014). In contrast to our findings, Zeng and Tice observed calcium-rich siderite or ankerite precipitation in experiments supplemented with calcium, and they did not report calcium carbonate mineralization. We hypothesize that the higher bioproduced aqueous ferrous iron concentrations enabled AFC (and siderite) to reach sufficient supersaturation for precipitation in the Zeng and Tice experiments, while the lower bioproduced Fe(II) concentrations in our experiments precluded the formation of these iron-rich carbonate minerals.

4.1.3 | Goethite

We identified secondary Fe(III) phases including goethite (α-FeOOH) in silica-free *S. putrefaciens* incubations, confirming Ferrozine results that indicated there was only partial reduction of the starting ferrihydrite substrate. This partial reduction occurred despite the excess electron donor (lactate) that was provided for *S. putrefaciens*. Secondary goethite mineralization arising from the microbial respiration of ferrihydrite is well documented (Bae & Lee, 2013; Fredrickson et al., 2001; Fredrickson et al., 2003; R. Han et al., 2018; Hansel et al., 2003; Pallud et al., 2010). Hansel et al. (2003) found that this secondary α-FeOOH mineralizes through dissolution and reprecipitation transformations of ferrihydrite during reactions with Fe(II), where sorbed Fe(II) passivates the ferrihydrite surface at low initial Fe(II) concentrations (<0.3 mM), inducing the mineralization of goethite instead of magnetite. After our 19 week incubations, the bioreduced solutions without silica had a mean [Fe(II)] of 0.34 mM (Figure 1; Table S3). Since the initial Fe(II) concentration was probably similar to control experiments (0.03 mM), increasing over time during bioreduction, goethite plausibly formed through this Fe(II)-induced reprecipitation pathway. In addition, we found further evidence of remnant Fe(III) with our tentative identifications of 6-line ferrihydrite and hematite alongside goethite in silica-free and magnesium-supplemented experiments (Figure 4c), suggesting there was an increase in particle size and crystallinity of the starting ferrihydrite substrate during microbial Fe(III) respiration.

In contrast, experiments augmented with silica did not form goethite. In fact, silica may inhibit goethite formation as it blocks the sorption of Fe(II) at reactive ferrihydrite surface sites (Jones et al., 2009; Schwertmann & Thalmann, 1976), subsequently stabilizing the ferrihydrite and hindering its transformation to other Fe-oxides (Anderson & Benjamin, 1985; Lee & Xu, 2019). As previously discussed, our results also suggest that released Fe(II) bonded with silica to form iron-silica coprecipitates. It is possible that the 'captured' Fe(II) in these siliceous coprecipitates limits Fe(II) interaction with remnant ferrihydrite. Regardless of the mechanism, the absence of goethite or detection of other secondary iron oxides in our silica-rich incubations suggests that the dissolved silica component prevented Fe(II)-induced solid state transformation of ferrihydrite to other Fe oxides (e.g., goethite, magnetite, hematite). Instead, our measurements showed siliceous experiments retained 13%–34% Fe(III) in solid products (Table S3), mainly as remnant two-line ferrihydrite that formed surfaces for iron-silica coprecipitation (e.g., Figure 4f).

4.2 | Implications for Precambrian BIFs

Microbial Fe(III) respiration likely influenced BIF deposition and/or the early stages of BIF diagenesis (Konhauser et al., 2005; Walker, 1984). One proposed mechanism for BIF formation argues for the deposition of primary iron oxides (e.g., ferrihydrite) (Beukes et al., 2008; Konhauser et al., 2017; LaBerge, 1964) that transformed into iron silicates, carbonates, magnetite, or other phases during iron bioreduction hosted in ancient sediments (Fischer & Knoll, 2009). We tested this hypothesis using laboratory simulations of *S. putrefaciens* suspensions in artificial Archean seawater to examine microbial iron reduction as a viable pathway for ancient iron silicate formation.

The carbonate minerals produced in our DIR incubations and control solutions, however, were unlike those recorded in early BIF assemblages. We observed pervasive calcium carbonate precipitation, and no evidence of iron carbonates—siderite or ankerite—that are ubiquitous in the BIF record (Klein, 2005; Trendall, 2002) and often attributed to dissimilatory iron reduction (Becker & Clayton, 1972; Heimann et al., 2010; Johnson et al., 2013; Mozley & Carothers, 1992; Walker, 1984). This $CaCO_3$ precipitation likely dominated due to inhibited iron carbonate growth kinetics and a low experimental Fe/Ca ratio with low total [Fe], conditions disparate from ancient sedimentary packages that hosted high concentrations of deposited iron precipitates. Hence, our experimental results are potentially more suitable for examining the mineral products from microbial iron respiration in an environment mimicking a water column containing dilute Fe(III) oxides. Furthermore, our observations of proliferate calcium carbonate forming in simulated Archean seawater conditions may imply that the deeper Archean ocean was actually less saturated with respect to calcium carbonate than our experimental conditions and/or that BIF depositional environments can be constrained to below the carbonate compensation depth (CCD).

Finally, our results demonstrate the precipitation of potential Fe(II)-rich proto-silicates from the microbial respiration of Fe(III) oxides. Although the experimental proto-silicates lack the well-layered structure of the greenalite particles hosted by Archean BIF cherts, the morphology of these phases is remarkably similar to 25°C, pH 7.5, proto-Fe(II,III) silicates that developed a coherent layered structure reminiscent of greenalite upon hydrothermal aging (Hinz et al., 2021). These comparable observations imply that the DIR-produced proto-silicate phases would evolve into more crystalline silicate minerals with simulated higher temperature diagenesis. However, even with a surplus of electron donor (lactate) and conditions apt for extensive Fe(III) respiration, we still observed substantial Fe(III) remaining in solids (Figure 1; Table S2). Given the Fe(III) content of the experimental solids, our findings may suggest that initial iron oxides would be preserved in the BIF record. Indeed, early nanoinclusions of hematite in 2.5 Ga Hamersley Group BIFs

reported by Sun, Konhauser, et al. (2015) and Li et al. (2013) could be relicts of a primary ferric oxyhydroxide. Notably, the average redox state of iron in BIFs is +2.4 (Klein & Beukes, 1992) and our most relevant experiments with calcium, magnesium, and silica produced solids with a final iron redox of 66% Fe(II)/FeT_{solid} or +2.3. The proximity of these experimental values with the BIF average composition may support the hypothesis that the partial reduction of initial ferric iron precipitates transpired during the genesis of BIF assemblages.

In contrast, Rasmussen et al. (2016, 2021) argue that the nanoscale ferric oxide particles are secondary to primary Fe(II) silicates (i.e., greenalite) based on textural relationships and paleomagnetic evidence that indicate iron oxides in BIFs formed during later stage fluid–rock interactions, metamorphism, and/or oxidative weathering (Muhling & Rasmussen, 2020; Rasmussen et al., 2021; Rasmussen et al., 2013, 2019, Rasmussen et al., 2016). We were unable to observe the extent of bioreduction necessary for the sole deposition of iron silicate mud after water column or sedimentary DIR, potentially due to restraints imposed by our nutrient-depleted medium (e.g. lacking phosphate and possible consumption of other essential trace elements) or the time limitation of our 19-week bioreduction incubations. However, investigating microbial Fe(III) respiration on more substantial timescales or with continuous chemostat cultures could possibly result in the complete reduction of ferrihydrite and singular production of Fe(II)-rich proto-silicates. While it is impossible to truly replicate the Archean ocean or ancient sedimentary porewaters in modern laboratory reconstructions, our experiments demonstrate that incipient iron silicates may have formed from microbial respiration of early ferric substrates, suggesting a possible alternative genesis for early BIF iron silicates.

ACKNOWLEDGMENTS

We would like to acknowledge funding from NASA Exobiology (J.E.J, Award #80NSSC18K1060) and the U-Michigan Department of Earth and Environmental Sciences Scott Turner Award Funds that supported this research. A special thanks to Alice Zhou for her assistance with culturing techniques and the spectrophotometric assays; Isaac Hinz for his insights on experimental set-up; and Daniel Zammit for his help with saturation index calculations. The authors acknowledge the Michigan Center for Materials Characterization, supported by the University of Michigan College of Engineering, for use of the instruments and staff assistance. We are especially grateful to Dr. Tao Ma for his mentorship on TEM operation and data analysis.

CONFLICTS OF INTEREST

The authors have no conflicts of interest to declare.

DATA AVAILABILITY STATEMENT

The data that supports the findings of this study are available in the supplementary material of this article.

ORCID

Christine Nims https://orcid.org/0000-0003-2636-7209
Jena E. Johnson https://orcid.org/0000-0001-8842-100X

REFERENCES

Anderson, P. R., & Benjamin, M. M. (1985). Effects of silicon on the crystallization and adsorption properties of ferric oxides. *Environmental Science and Technology*, *19*(11), 1048–1053. https://doi.org/10.1021/es00141a004

Bae, S., & Lee, W. (2013). Biotransformation of lepidocrocite in the presence of quinones and flavins. *Geochimica et Cosmochimica Acta*, *114*, 144–155. https://doi.org/10.1016/j.gca.2013.03.041

Balch, W. E., & Wolfe, R. S. (1976). New approach to the cultivation of methanogenic bacteria: 2 mercaptoethanesulfonic acid (HS CoM) dependent growth of *Methanobacterium ruminantium* in a pressurized atmosphere. *Applied and Environmental Microbiology*, *32*(6), 781–791. https://doi.org/10.1128/aem.32.6.781-791.1976

Baur, M. E., Hayes, J. M., Studley, S. A., & Walter, M. R. (1985). Millimeter-scale variations of stable isotope abundances in carbonates from Banded Iron-Formations in the Hamersley Group of Western Australia. *Economic Geology*, *80*(2), 270–282. https://doi.org/10.2113/gsecongeo.80.2.270

Becker, R. H.,& Clayton, N. R. (1972). Carbon isotopic evidence for the origin of a banded iron-formation in Western Australia. *Geochimica et Cosmochimica Acta*, *36*(5), 577–595. https://doi.org/10.1016/0016-7037(72)90077-4

Bekker, A., Krapež, B., Slack, J. F., Planavsky, N., Hofmann, A., Konhauser, K. O., & Rouxel, O. J. (2010). Iron formation: The sedimentary product of a complex interplay among mantle, tectonic, oceanic, and biospheric processes-a reply. *Economic Geology*, *107*(2), 379–380. https://doi.org/10.2113/econgeo.107.2.379

Bekker, A., Planavsky, N. J., Krapež, B., Rasmussen, B., Hofmann, A., Slack, J. F., Rouxel, O., & Konhauser, K. O. (2014). Iron formations: Their origins and implications for ancient seawater chemistry. In *Treatise on geochemistry* (Vol. *9*, 2nd ed., pp. 561–628). Elsevier.

Bergmann, K. D., Grotzinger, J. P., & Fischer, W. W. (2013). Biological influences on seafloor carbonate precipitation. *Palaios*, *28*(2), 99–115. https://doi.org/10.2110/palo.2012.p12-088r

Berner, R. A. (1975). The role of magnesium in the crystal growth of calcite and aragonite from sea water. *Geochimica et Cosmochimica Acta*, *39*, 489–504.

Beukes, N. J., Mukhopadhyay, J., & Gutzmer, J. (2008). Genesis of high-grade iron ores of the Archean Iron Ore Group around Noamundi, India. *Economic Geology*, *103*(2), 365–386. https://doi.org/10.2113/gsecongeo.103.2.365

Biffinger, J. C., Pietron, J., Bretschger, O., Nadeau, L. J., Johnson, G. R., Williams, C. C., Nealson, K. H., & Ringeisen, B. R. (2008). The influence of acidity on microbial fuel cells containing *Shewanella oneidensis*. *Biosensors and Bioelectronics*, *24*(4), 900–905. https://doi.org/10.1016/j.bios.2008.07.034

Busenberg, E., & Plummer, L. N. (1986). A comparative study of the dissolution and crystal growth kinetics of calcite and aragonite. *US Geological Survey Bulletin*, *1578*, 139–168.

Cismasu, A. C., Levard, C., Michel, F. M., & Brown, G. E. (2013). Properties of impurity-bearing ferrihydrite II: Insights into the surface structure and composition of pure, Al- and Si-bearing ferrihydrite from Zn(II) sorption experiments and Zn K-edge X-ray absorption spectroscopy. *Geochimica et Cosmochimica Acta*, *119*, 46–60. https://doi.org/10.1016/j.gca.2013.05.040

Craddock, P. R., & Dauphas, N. (2011). Iron and carbon isotope evidence for microbial iron respiration throughout the Archean. *Earth and Planetary Science Letters*, *303*(1–2), 121–132. https://doi.org/10.1016/j.epsl.2010.12.045

Davis, K. J., Dove, P. M., & De Yoreo, J. J. (2000). The role of Mg^{2+} as an impurity in calcite growth. *Science*, *290*(5494), 1134–1137. https://doi.org/10.1126/science.290.5494.1134

Di Lorenzo, F., Burgos-Cara, A., Ruiz-Agudo, E., Putnis, C. V., & Prieto, M. (2017). Effect of ferrous iron on the nucleation and growth of $CaCO_3$ in slightly basic aqueous solutions. *CrystEngComm*, *19*(3), 447–460. https://doi.org/10.1039/c6ce02290a

Dong, H., Jaisi, D. P., Kim, J., & Zhang, G. (2009). Microbe-clay mineral interactions. *American Mineralogist*, *94*(11–12), 1505–1519. https://doi.org/10.2138/am.2009.3246

Dromgoole, E. L., & Walter, L. M. (1990). Iron and manganese incorporation into calcite: Effects of growth kinetics, temperature and solution chemistry. *Chemical Geology*, *81*(4), 311–336. https://doi.org/10.1016/0009-2541(90)90053-A

Etique, M., Jorand, F. P. A., & Ruby, C. (2016). Magnetite as a precursor for green rust through the hydrogenotrophic activity of the iron-reducing bacteria *Shewanella putrefaciens*. *Geobiology*, *14*(3), 237–254. https://doi.org/10.1111/gbi.12170

Farquhar, J., Nanping, W. U., Canfield, D. E., & Oduro, H. (2010). Connections between sulfur cycle evolution, sulfur isotopes, sediments and base metal sulfide deposits. *Economic Geology*, *105*(3), 509–533. https://doi.org/10.2113/gsecongeo.105.3.509

Fischer, W. W., & Knoll, A. H. (2009). An iron shuttle for deepwater silica in late Archean and early Paleoproterozoic iron formation. *Bulletin of the Geological Society of America*, *121*(1–2), 222–235. https://doi.org/10.1130/B26328.1

Frankel, G. S., Vienna, J. D., Lian, J., Scully, J. R., Gin, S., Ryan, J. V., Wang, J., Kim, S. H., Windl, W., & Du, J. (2018). A comparative review of the aqueous corrosion of glasses, crystalline ceramics, and metals. *NPJ Materials Degradation*, *2*(1), 15. https://doi.org/10.1038/s41529-018-0037-2

Fredrickson, J. K., Kota, S., Kukkadapu, R. K., Liu, C., & Zachara, J. M. (2003). Influence of electron donor/acceptor concentrations on hydrous ferric oxide (HFO) bioreduction. *Biodegradation*, *14*(2), 91–103. https://doi.org/10.1023/A:1024001207574

Fredrickson, J. K., Zachara, J. M., Kukkadapu, R. K., Gorby, Y. A., Smith, S. C., & Brown, C. F. (2001). Biotransformation of Ni-substituted hydrous ferric oxide by an Fe(III)-reducing bacterium. *Environmental Science and Technology*, *35*(4), 703–712. https://doi.org/10.1021/es001500v

Fredrickson, J. K., Zachara, J. M., Kennedy, D. W., Dong, H., Onstott, T. C., Hinman, N. W., & Li, S. M. (1998). Biogenic iron mineralization accompanying the dissimilatory reduction of hydrous ferric oxide by a groundwater bacterium. *Geochimica et Cosmochimica Acta*, *62*(19–20), 3239–3257. https://doi.org/10.1016/S0016-7037(98)00243-9

Glasauer, S., Langley, S., & Beveridge, T. J. (2001). Sorption of Fe (Hydr) Oxides to the surface of *Shewanella putrefaciens*: Cell-bound fine-grained minerals are not always formed de novo. *Applied and Environmental Microbiology*, *67*(12), 5544–5550. https://doi.org/10.1128/AEM.67.12.5544-5550.2001

Glasauer, S., Langley, S., Boyanov, M., Lai, B., Kemner, K., & Beveridge, T. J. (2007). Mixed-valence cytoplasmic iron granules are linked to anaerobic respiration. *Applied and Environmental Microbiology*, *73*(3), 993–996. https://doi.org/10.1128/AEM.01492-06

Glasauer, S., Langley, S., & Beveridge, T. J. (2002). Intracellular iron minerals in a dissimilatory iron-reducing bacterium. *Science*, *295*(5552), 117–119.

Halevy, I., & Bachan, A. (2017). The geologic history of seawater pH. *Science*, *355*(6329), 1069–1071. https://doi.org/10.1126/science.aal4151

Han, R., Liu, T., Li, F., Li, X., Chen, D., & Wu, Y. (2018). Dependence of secondary mineral formation on Fe(II) production from ferrihydrite reduction by *Shewanella oneidensis* MR-1. *ACS Earth and Space Chemistry*, *2*(4), 399–409. https://doi.org/10.1021/acsearthspacechem.7b00132

Han, X., Tomaszewski, E. J., Sorwat, J., Pan, Y., Kappler, A., & Byrne, J. M. (2020). Effect of microbial biomass and humic acids on abiotic and biotic magnetite formation. *Environmental Science and Technology*, *54*(7), 4121–4130. https://doi.org/10.1021/acs.est.9b07095

Hansel, C. M., Benner, S. G., Neiss, J., Dohnalkova, A., Kukkadapu, R. K., & Fendorf, S. (2003). Secondary mineralization pathways induced by dissimilatory iron reduction of ferrihydrite under advective flow. *Geochimica et Cosmochimica Acta*, *67*(16), 2977–2992. https://doi.org/10.1016/S0016-7037(03)00276-X

Harder, H. (1978). Synthesis of iron layer silicate minerals under natural conditions. *Clays and Clay Minerals*, *26*(1), 65–72. https://doi.org/10.1346/CCMN.1978.0260108

Heimann, A., Johnson, C. M., Beard, B. L., Valley, J. W., Roden, E. E., Spicuzza, M. J., & Beukes, N. J. (2010). Fe, C, and O isotope compositions of banded iron formation carbonates demonstrate a major role for dissimilatory iron reduction in ~2.5Ga marine environments. *Earth and Planetary Science Letters*, *294*(1–2), 8–18. https://doi.org/10.1016/j.epsl.2010.02.015

Higgins, J. A., Fischer, W. W., & Schrag, D. P. (2009). Oxygenation of the ocean and sediments: Consequences for the seafloor carbonate factory. *Earth and Planetary Science Letters*, *284*(1–2), 25–33. https://doi.org/10.1016/j.epsl.2009.03.039

Hinz, I. L., Nims, C., Theuer, S., Templeton, A. S., & Johnson, J. E. (2021). Ferric iron triggers greenalite formation in simulated Archean seawater. *Geology*, *49*, 905–910. https://doi.org/10.1130/g48495.1

Holland, H. D. (1984). *The chemical evolution of the atmosphere and ocean*. Princeton University Press.

Janney, D. E., Cowley, J. M., & Buseck, P. R. (2000). Transmission electron microscopy of synthetic 2- and 6-line ferrihydrite. *Clays and Clay Minerals*, *48*(1), 111–119. https://doi.org/10.1346/CCMN.2000.0480114

Jiang, C. Z., & Tosca, N. J. (2019). Fe(II)-carbonate precipitation kinetics and the chemistry of anoxic ferruginous seawater. *Earth and Planetary Science Letters*, *506*, 231–242. https://doi.org/10.1016/j.epsl.2018.11.010

Jiang, C. Z., & Tosca, N. J. (2020). Growth kinetics of siderite at 298.15 K and 1 bar. *Geochimica et Cosmochimica Acta*, *274*, 97–117. https://doi.org/10.1016/j.gca.2020.01.047

Johnson, C. M., Beard, B. L., & Roden, E. E. (2008). The iron isotope fingerprints of redox and biogeochemical cycling in modern and ancient earth. *Annual Review of Earth and Planetary Sciences*, *36*, 457–493. https://doi.org/10.1146/annurev.earth.36.031207.124139

Johnson, C. M., Ludois, J. M., Beard, B. L., Beukes, N. J., & Heimann, A. (2013). Iron formation carbonates: Paleoceanographic proxy or recorder of microbial diagenesis? *Geology*, *41*(11), 1147–1150. https://doi.org/10.1130/G34698.1

Johnson, J. E. (2019). From minerals to metabolisms: Evidence for life before oxygen from the geological record. *Free Radical Biology and Medicine*, *140*, 126–137. https://doi.org/10.1016/j.freeradbiomed.2019.01.047

Johnson, J. E., & Molnar, P. H. (2019). Widespread and persistent deposition of iron formations for two billion years. *Geophysical Research Letters*, *46*(6), 3327–3339. https://doi.org/10.1029/2019GL081970

Johnson, J. E., Muhling, J. R., Cosmidis, J., Rasmussen, B., & Templeton, A. S. (2018). Low-Fe(III) greenalite was a primary mineral from Neoarchean oceans. *Geophysical Research Letters*, *45*(7), 3182–3192. https://doi.org/10.1002/2017GL076311

Jones, A. M., Collins, R. N., Rose, J., & Waite, T. D. (2009). The effect of silica and natural organic matter on the Fe(II)-catalysed transformation and reactivity of Fe(III) minerals. *Geochimica et Cosmochimica Acta*, *73*(15), 4409–4422. https://doi.org/10.1016/j.gca.2009.04.025

Jones, C., Nomosatryo, S., Crowe, S. A., Bjerrum, C. J., & Canfield, D. E. (2015). Iron oxides, divalent cations, silica, and the early earth phosphorus crisis. *Geology*, *43*(2), 135–138. https://doi.org/10.1130/G36044.1

Jorand, F., Appenzeller, B. M. R., Abdelmoula, M., Refait, P., Block, J. C., & Genin, J.-M. R. (2000). Assessment of vivianite formation in *Shewanella putrefaciens* culture. *Environmental Technology*, *21*(9), 1001–1005.

Kato, S., Itoh, T., Yuki, M., Nagamori, M., Ohnishi, M., Uematsu, K., Suzuki, K., Takashina, T., & Ohkuma, M. (2019). Isolation and characterization of a thermophilic sulfur- and iron-reducing thaumarchaeote from a terrestrial acidic hot spring. *ISME Journal*, *13*(10), 2465–2474. https://doi.org/10.1038/s41396-019-0447-3

Kellermeier, M., Glaab, F., Klein, R., Melero-García, E., Kunz, W., & García-Ruiz, J. M. (2013). The effect of silica on polymorphic precipitation of calcium carbonate: An on-line energy-dispersive X-ray diffraction (EDXRD) study. *Nanoscale*, *5*(15), 7054–7065. https://doi.org/10.1039/c3nr00301a

Kinsela, A. S., Jones, A. M., Bligh, M. W., Pham, A. N., Collins, R. N., Harrison, J. J., Wilsher, K. L., Payne, T. E., & Waite, T. D. (2016). Influence of dissolved silicate on rates of Fe(II) oxidation. *Environmental Science and Technology*, *50*(21), 11663–11671. https://doi.org/10.1021/acs.est.6b03015

Klein, C. (2005). Some Precambrian banded iron-formations (BIFs) from around the world: Their age, geologic setting, mineralogy, metamorphism, geochemistry, and origin. *American Mineralogist*, *90*(10), 1473–1499. https://doi.org/10.2138/am.2005.1871

Klein, C., & Beukes, N. J. (1992). Time distribution, stratigraphy, and sedimentologic setting,and geochemistry of Precambrian iron-formation. In J. W. Schopf & C. Klein (Eds.), *The proterozoic biosphere: A multidisciplinary study* (pp. 139–146). Cambridge University Press.

Knoll, A. H., Bergmann, K. D., & Strauss, J. V. (2016). Life: The first two billion years. *Philosophical Transactions of the Royal Society B: Biological Sciences*, *371*(1707), 20150493. https://doi.org/10.1098/rstb.2015.0493

Komlos, J., Kukkadapu, R. K., Zachara, J. M., & Jaffé, P. R. (2007). Biostimulation of iron reduction and subsequent oxidation of sediment containing Fe-silicates and Fe-oxides: Effect of redox cycling on Fe(III) bioreduction. *Water Research*, *41*(13), 2996–3004. https://doi.org/10.1016/j.watres.2007.03.019

Konhauser, K., Newman, D., & Kappler, A. (2005). The potential significance of microbial Fe (III) reduction. *Geobiology*, *3*, 167–177.

Konhauser, K. O., Planavsky, N. J., Hardisty, D. S., Robbins, L. J., Warchola, T. J., Haugaard, R., Lalonde, S. V., Partin, C. A., Oonk, P. B. H., Tsikos, H., Lyons, T. W., Bekker, A., & Johnson, C. M. (2017). Iron formations: A global record of Neoarchaean to Palaeoproterozoic environmental history. *Earth-Science Reviews*, *172*, 140–177. https://doi.org/10.1016/j.earscirev.2017.06.012

Konhauser, K. O., Amskold, L., Lalonde, S. V., Posth, N. R., Kappler, A., & Anbar, A. (2007). Decoupling photochemical Fe(II) oxidation from shallow-water BIF deposition. *Earth and Planetary Science Letters*, *258*(1–2), 87–100. https://doi.org/10.1016/j.epsl.2007.03.026

Kostka, J. E., Haefele, E., Viehweger, R., & Stucki, J. W. (1999). Respiration and dissolution of iron(III)-containing clay minerals by bacteria. *Environmental Science and Technology*, *33*(18), 3127–3133. https://doi.org/10.1021/es990021x

Krapež, B., Barley, M. E., & Pickard, A. L. (2003). Hydrothermal and resedimented origins of the precursor sediments to banded iron formation: Sedimentological evidence from the Early Palaeoproterozoic Brockman Supersequence of Western Australia. *Sedimentology*, *50*(5), 979–1011. https://doi.org/10.1046/j.1365-3091.2003.00594.x

Krissansen-Totton, J., Arney, G. N., & Catling, D. C. (2018). Constraining the climate and ocean pH of the early Earth with a geological carbon cycle model. *Proceedings of the National Academy of Sciences of the United States of America*, *115*(16), 4105–4110. https://doi.org/10.1073/pnas.1721296115

Kukkadapu, R. K., Zachara, J. M., Fredrickson, J. K., & Kennedy, D. W. (2004). Biotransformation of two-line silica-ferrihydrite by a dissimilatory Fe(III)-reducing bacterium: Formation of carbonate green rust in the presence of phosphate. *Geochimica et Cosmochimica Acta*, *68*(13), 2799–2814. https://doi.org/10.1016/j.gca.2003.12.024

LaBerge, G. (1964). Development of magnetite in iron formations of the Lake superior region. *Economic Geology*, *59*, 1313–1342. https://doi.org/10.2113/gsecongeo.61.2.408

Lafuente, B., Downs, R. T., Yang, H., & Stone, N. (2016). The power of databases: The RRUFF project. In *Highlights in mineralogical crystallography* (pp. 1–30). https://www.degruyter.com/document/doi/10.1515/9783110417104-003/html

Lee, S., & Xu, H. (2019). One-Step route synthesis of siliceous six-line ferrihydrite: Implication for the formation of natural ferrihydrite. *ACS Earth and Space Chemistry*, *3*(4), 503–509. https://doi.org/10.1021/acsearthspacechem.8b00179

Lepot, K., Addad, A., Knoll, A. H., Wang, J., Troadec, D., Béché, A., & Javaux, E. J. (2017). Iron minerals within specific microfossil morphospecies of the 1.88 Ga Gunflint Formation. *Nature Communications*, *8*, 14890. https://doi.org/10.1038/ncomms14890

Li, Y. L., Cole, D. R., Konhauser, K., & Chan, L. S. (2013). Quartz nanocrystals in the 2.48 Ga Dales Gorge banded iron formation of Hamersley, Western Australia: Evidence for a change from submarine to subaerial volcanism at the end of the Archean. *American Mineralogist*, *98*(4), 582–587. https://doi.org/10.2138/am.2013.4205

Lovley, D. R., & Phillips, E. J. P. (1988). Novel mode of microbial energy metabolism: Organic carbon oxidation coupled to dissimilatory reduction of iron or manganese. *Applied and Environmental Microbiology*, *54*(6), 1472–1480. https://doi.org/10.1128/aem.54.6.1472-1480.1988

Lyu, J., Qin, W., Zhang, C., & Li, F. (2020). Nanoparticle accumulation in microbial induced carbonate precipitation: The crucial role of extracellular polymeric substance. *Geomicrobiology Journal*, *37*, 837–847. https://doi.org/10.1080/01490451.2020.1786866

Maliva, R. G., Knoll, A. H., & Simonson, B. M. (2005). Secular change in the Precambrian silica cycle: Insights from chert petrology. *Bulletin of the Geological Society of America*, *117*, 835–845. https://doi.org/10.1130/B25555.1

McLean, J. S., Pinchuk, G. E., Geydebrekht, O. V., Bilskis, C. L., Zakrajsek, B. A., Hill, E. A., Saffarini, D. A., Romine, M. F., Gorby, Y. A., Fredrickson, J. K., & Beliaev, A. S. (2008). Oxygen-dependent autoaggregation in *Shewanella oneidensis* MR-1. *Environmental Microbiology*, *10*(7), 1861–1876. https://doi.org/10.1111/j.1462-2920.2008.01608.x

Meyer, H. J. (1984). The influence of impurities on the growth rate of calcite. *Journal of Crystal Growth*, *66*(3), 639–646. https://doi.org/10.1016/0022-0248(84)90164-7

Michalopoulos, P., & Aller, R. C. (1995). Rapid clay mineral formation in Amazon delta sediments: Reverse weathering and oceanic elemental cycles. *American Association for the Advancement of Science Stable*, *270*(5236), 614–617.

Miot, J., & Etique, M. (2016). Formation and transformation of iron-bearing minerals by iron(II)-oxidizing and iron(III)-reducing bacteria. In D. Faivre (Ed.), *Iron oxides: From nature to applications* (pp. 53–97). Wiley-VCH.

Mozley, P. S., & Carothers, W. W. (1992). Elemental and isotopic composition of siderite in the Kuparuk Formation, Alaska: Effect of microbial activity and water/sediment interaction on early pore-water chemistry. *Journal of Sedimentary Petrology*, *62*(4), 681–692. https://doi.org/10.1306/D4267988-2B26-11D7-8648000102C1865D

Mucci, A., & Morse, J. W. (1982). The incorporation of divalent Mg and divalent Sr into calcite overgrowths: Influences of growth rate and solution composition. *Geochimica et Cosmochimica Acta*, *47*, 217–233.

Muhling, J. R., & Rasmussen, B. (2020). Widespread deposition of greenalite to form Banded Iron Formations before the Great Oxidation Event. *Precambrian Research*, *339*, 105619. https://doi.org/10.1016/j.precamres.2020.105619

Myers, C. R., & Nealson, K. H. (1990). Respiration-linked proton translocation couples to anaerobic reduction of manganese(IV) and iron(III) in *Shewanella putrefaciens* MR-1. *Journal of Bacteriology*, *172*(11), 6232–6238. https://doi.org/10.1128/jb.172.11.6232-6238.1990

O'Loughlin, E. J., Gorski, C. A., Flynn, T. M., & Scherer, M. M. (2019). Electron donor utilization andsecondary mineral formation during the bioreduction of lepidocrocite by *Shewanella putrefaciens* CN32. *Minerals*, *9*(7), 434. https://doi.org/10.3390/min9070434

O'Reilly, S. E. (2005). Secondary mineral formation associated with respiration of nontronite, NAu-1 by iron reducing bacteria. *Geochemical Transactions*, *6*(4), 67. https://doi.org/10.1063/1.2084787

Pakchung, A. A. H., Soe, C. Z., & Codd, R. (2008). Studies of iron-uptake mechanisms in two bacterial species of the *Shewanella* genus adapted to middle-range (*Shewanella putrefaciens*) or Antarctic (*Shewanella gelidimarina*) temperatures. *Chemistry and Biodiversity*, *5*(10), 2113–2123. https://doi.org/10.1002/cbdv.200890192

Pallud, C., Masue-Slowey, Y., & Fendorf, S. (2010). Aggregate-scale spatial heterogeneity in reductive transformation of ferrihydrite resulting from coupled biogeochemical and physical processes. *Geochimica et Cosmochimica Acta*, *74*(10), 2811–2825. https://doi.org/10.1016/j.gca.2010.01.032

Percak-Dennet, E. M., Beard, B. L., Xu, H., Konishi, H., Johnson, C. M., & Roden, E. E. (2011). Iron isotope fractionation during microbial dissimilatory iron oxide reduction in simulated Archaean seawater. *Geobiology*, *9*, 205–220. https://doi.org/10.1111/j.1472-4669.2011.00277.x

Phoenix, V. R., Konhauser, K. O., & Ferris, F. G. (2003). Experimental study of iron and silica immobilization by bacteria in mixed Fe-Si systems: Implications for microbial silicification in hot springs. *Canadian Journal of Earth Sciences*, *40*(11), 1669–1678. https://doi.org/10.1139/e03-044

Poulton, S. W., & Canfeld, D. E. (2011). Ferruginous conditions: A dominant feature of the ocean through Earth's history. *Elements*, *7*(2), 107–112. https://doi.org/10.2113/gselements.7.2.107

Rasmussen, B., Krapež, B., & Meier, D. B. (2014). Replacement origin for hematite in 2.5 Ga banded iron formation: Evidence for postdepositional oxidation of iron-bearing minerals. *Bulletin of the Geological Society of America*, *126*(3–4), 438–446. https://doi.org/10.1130/B30944.1

Rasmussen, B., Krapež, B., & Muhling, J. R. (2015). Seafloor silicification and hardground development during deposition of 2.5 Ga banded iron formations. *Geology*, *43*(3), 235–238. https://doi.org/10.1130/G36363.1

Rasmussen, B., Krapež, B., Muhling, J. R., & Suvorova, A. (2015). Precipitation of iron silicate nanoparticles in early Precambrian oceans marks Earth's first iron age. *Geology*, *43*, 303–306. https://doi.org/10.1130/G36309.1

Rasmussen, B., Meier, D. B., Krapež, B., & Muhling, J. R. (2013). Iron silicate microgranules as precursor sediments to 2.5-billion-yearold banded iron formations. *Geology*, *41*(4), 435–438. https://doi.org/10.1130/G33828.1

Rasmussen, B., Muhling, J. R., & Fischer, W. W. (2019). Evidence from laminated chert in banded iron formations for deposition by gravitational settling of iron-silicate muds. *Geology*, *47*(2), 167–170. https://doi.org/10.1130/G45560.1

Rasmussen, B., Muhling, J. R., & Krapež, B. (2021). Greenalite and its role in the genesis of early Precambrian iron formations – A review. *Earth-Science Reviews*, *217*, 103613. https://doi.org/10.1016/j.earscirev.2021.103613

Rasmussen, B., Muhling, J. R., Suvorova, A., & Krapež, B. (2016). Dust to dust: Evidence for the formation of "primary" hematite dust in banded iron formations via oxidation of iron silicate nanoparticles. *Precambrian Research*, *284*, 49–63. https://doi.org/10.1016/j.precamres.2016.07.003

Reddy, T. R., Zheng, X. Y., Roden, E. E., Beard, B. L., & Johnson, C. M. (2016). Silicon isotope fractionation during microbial reduction of Fe(III)–Si gels under Archean seawater conditions and implications for iron formation genesis. *Geochimica et Cosmochimica Acta*, *190*, 85–99. https://doi.org/10.1016/j.gca.2016.06.035

Robbins, L. J., Funk, S. P., Flynn, S. L., Warchola, T. J., Li, Z., Lalonde, S. V., Rostron, B. J., Smith, A. J. B., Beukes, N. J., de Kock, M. O., Heaman, L. M., Alessi, D. S., & Konhauser, K. O. (2019). Hydrogeological constraints on the formation of Palaeoproterozoic banded iron formations. *Nature Geoscience*, *12*(7), 558–563. https://doi.org/10.1038/s41561-019-0372-0

Roden, E. E., & Urrutia, M. M. (2002). Influence of biogenic Fe(II) on bacterial crystalline Fe(III) oxide reduction. *Geomicrobiology Journal*, *19*(2), 209–251. https://doi.org/10.1080/01490450252864280

Salas, E. C., Berelson, W. M., Hammond, D. E., Kampf, A. R., & Nealson, K. H. (2009). The influence of carbon source on the products of dissimilatory iron reduction. *Geomicrobiology Journal*, *26*(7), 451–462. https://doi.org/10.1080/01490450903060806

Schwertmann, U., & Thalmann, H. (1976). The Influence of [Fe(II)], [Si], and pH on the formation of lepidocrocite and ferrihydrite during oxidation of aqueous FeCl 2 solutions. *Clay Minerals*, *11*(3), 189–200. https://doi.org/10.1180/claymin.1976.011.3.02

Sergent, A. S., Jorand, F., & Hanna, K. (2011). Effects of Si-bearing minerals on the nature of secondary iron mineral products from lepidocrocite bioreduction. *Chemical Geology*, *289*(1–2), 86–97. https://doi.org/10.1016/j.chemgeo.2011.07.016

Siever, R. (1992). The silica cycle in the Precambrian. *Geochimica et Cosmochimica Acta*, *56*(8), 3265–3272. https://doi.org/10.1016/0016-7037(92)90303-z

Sklute, E. C., Kashyap, S., Dyar, M. D., Holden, J. F., Tague, T., Wang, P., & Jaret, S. J. (2018). Spectral and morphological characteristics of synthetic nanophase iron (oxyhydr)oxides. *Physics and Chemistry of Minerals*, *45*(1), 1–26. https://doi.org/10.1007/s00269-017-0897-y

Stookey, L. L. (1970). Ferrozine – a new spectrophotometric reagent for iron. *Analytical Chemistry*, *42*(7), 779–781. https://doi.org/10.1021/ac60289a016

Sun, S., Konhauser, K. O., Kappler, A., & Li, Y. L. (2015). Primary hematite in Neoarchean to Paleoproterozoic oceans. *Bulletin of the Geological Society of America*, *127*(5–6), 850–861. https://doi.org/10.1130/B31122.1

Sun, W., Jayaraman, S., Chen, W., Persson, K. A., & Ceder, G. (2015). Correction: Nucleation of metastable aragonite CaCO3in seawater (Proceedings of the National Academy of Sciences of The United States of America (2015), 112:3199–3204 (DOI: 10.1073/pnas.1423898112)). *Proceedings of the National Academy of Sciences of the United States of America*, *112*(20), E2735. https://doi.org/10.1073/pnas.1506100112

Swedlund, P., & Webster, J. (1999). Adsorption and polymerisation of silicic acid on ferrihydrite, and its effect on arsenic adsorption. *Water Research*, *33*(16), 3413–3422. https://doi.org/10.1016/S0043-1354(99)00055-X

Tosca, N. J., Guggenheim, S., & Pufahl, P. K. (2016). An authigenic origin for Precambrian greenalite: Implications for iron formation and the chemistry of ancient seawater. *Bulletin of the Geological Society of America*, *128*(3–4), 511–530. https://doi.org/10.1130/B31339.1

Tosca, N. J., Jiang, C. Z., Rasmussen, B., & Muhling, J. (2019). Products of the iron cycle on the early Earth. *Free Radical Biology and Medicine*, *140*(April), 138–153. https://doi.org/10.1016/j.freeradbiomed.2019.05.005

Trendall, A. F. (2002). The significance of iron-formation in the precambrian stratigraphic record. In W. Altermann & P. L. Corcoran (Eds.), *Precambrian sedimentary environments* (pp. 33–66). International Association of Sedimentologists Special Publications.

Viollier, E., Inglett, P. W., Hunter, K., Roychoudhury, A. N., & Van Cappellen, P. (2000). The Ferrozine method revisted. *Applied Geochemistry*, *15*, 785–790.

Virdis, B., Millo, D., Donose, B. C., & Batstone, D. J. (2014). Real-time measurements of the redox states of c-type cytochromes in

electroactive biofilms: A confocal resonance raman microscopy study. *PLoS One*, *9*(2), e89918. https://doi.org/10.1371/journal.pone.0089918

Wacey, D., Saunders, M., Roberts, M., Menon, S., Green, L., Kong, C., Culwick, T., Strother, P., & Brasier, M. D. (2014). Enhanced cellular preservation by clay minerals in 1 billion-year-old lakes. *Scientific Reports*, *4*, 1–12. https://doi.org/10.1038/srep05841

Walker, J. C. G. (1984). Suboxic diagenesis in banded iron formations. *Nature*, *309*(5966), 340–342. https://doi.org/10.1038/309340a0

Widdel, F., Kohring, G.-W., & Mayer, F. (1983). Studies on dissimilatory sulfate-reducing bacteria that decompose fatty acids. *Archives of Microbiology*, *134*(4), 286–294. https://doi.org/10.1007/bf00407804

Wolf, M. W., Rizzolo, K., Elliott, S. J., & Lehnert, N. (2018). Resonance Raman, electron paramagnetic resonance, and magnetic circular dichroism spectroscopic investigation of diheme cytochrome *c* peroxidases from *Nitrosomonas europaea* and *Shewanella oneidensis*. *Biochemistry*, *57*(45), 6416–6433. https://doi.org/10.1021/acs.biochem.8b00732

Wu, L., Beard, B. L., Roden, E. E., & Johnson, C. M. (2009). Influence of pH and dissolved Si on Fe isotope fractionation during dissimilatory microbial reduction of hematite. *Geochimica et Cosmochimica Acta*, *73*(19), 5584–5599. https://doi.org/10.1016/j.gca.2009.06.026

Zachara, J. M., Kukkadapu, R. K., Fredrickson, J. K., Gorby, Y. A., & Smith, S. C. (2002). Biomineralization of poorly crystalline Fe(III) oxides by dissimilatory metal reducing bacteria (DMRB). *Geomicrobiology Journal*, *19*(2), 179–207. https://doi.org/10.1080/01490450252864271

Zegeye, A., Mustin, C., & Jorand, F. (2010). Bacterial and iron oxide aggregates mediate secondary iron mineral formation: Green rust versus magnetite. *Geobiology*, *8*(3), 209–222. https://doi.org/10.1111/j.1472-4669.2010.00238.x

Zeller, E. J., & Wray, J. (1956). Factors influencing precipitation of calcium carbonate. *AAPG Bulletin*, *40*(1), 140–152. https://doi.org/10.1306/5ceae30a-16bb-11d7-8645000102c1865d

Zeng, Z., & Tice, M. M. (2014). Promotion and nucleation of carbonate precipitation during microbial iron reduction. *Geobiology*, *12*(4), 362–371. https://doi.org/10.1111/gbi.12090

SUPPORTING INFORMATION

Additional supporting information can be found online in the Supporting Information section at the end of this article.

How to cite this article: Nims, C., & Johnson, J. E. (2022). Exploring the secondary mineral products generated by microbial iron respiration in Archean ocean simulations. *Geobiology*, *20*, 743–763. https://doi.org/10.1111/gbi.12523